Mechanical and Industrial Engineering

5 papers

A Model for End-of-Life Vehicles Management based on Green Manufacturing

Aman Chitrakar, Liu Fei, Cao HuaJun, He Yan

Institute of Manufacturing Engineering, Chongqing University, Chongqing 400044, P.R. China
Email: amanchitrakar@yahoo.com / ORCID ID: 0009-0004-4824-2452

Abstract

Like any industrial product, the vehicles also do have end to their service lives and ultimately result into end-of-life vehicle (ELV) at a certain stage of the vehicle life. The concern of this paper is to make a general review on ELV management process and present a model for ELV management on the basis of green manufacturing so as to reduce the environmental impact and minimize the resources loss due to the ELVs. The various phases of vehicle life cycle starting from design, manufacturing and utilization, occurrence of ELV and then the storage, depollution, dismantling and finally the shredding and post shredder material processing phases of ELV for the resource's recovery, all of these phases need to be considered to give totality to end-of-life vehicle management.

Keywords: End-of-Life Vehicles (ELVs), Green Manufacturing, Circular Economy, Sustainable Vehicle Industry, Environmental Management.

1. Introduction

With the increase in the number of vehicles being used in our human society, the numbers of vehicles arriving at their end-of-life stage are also in increase and merely by the general observation it is seen that this increment is in direct proportion with the economic development of the society in most parts of the world. In the context of the issuance of ELV management directives by EU [3], the management of ELV should be handled more stringently and the perspective of similar regulation is quite likely to be implemented by many other countries in near future. Hence, the challenge of managing the waste generated by the end-of-life vehicles (ELVs) is of great significance and should be taken proper care of in order to have a better tomorrow from environmental point of view.

The major issue for ELV management (ELVM) based on green manufacturing is how to manage these ELVs with least environmental hazard and resource loss. Potentially ELV's environmental impacts fall into two main categories- Pollution & Resource Loss [1]. The improper disposal of ELVs gives rise to the possibility of operating fluids (oil, petrol, brake and transmission fluids etc) and other potentially harmful materials to be released into the environment. Improperly stored vehicles and components may also cause other environmental problems, including visual pollution, disruption to watercourses, and result in vermin breeding etc. In addition to the direct pollution impact, there could be a significant environmental cost due to the resource loss from the ELV not being recycled to extent possible or commercially viable.

The ELV management task has two sides that need to be taken care of:

1) the management of the vehicles that has already arrived at end of their service lives in order to retrieve the useful resources from them and lessen the environmental impact due to the disposal of irretrievable materials.

2) the management during production and utilization phases prior to ELV stage so as to make easy recovery and disposal of materials from the end of vehicles at the end of their service lives.

Not only the ELV remained as a single unit body after use needs to be managed but also the spare parts (including consumables, service and broken down parts) that have been damaged or were due for replacement and hence replaced during the operational life of vehicle are also the major issues that is to be taken care of since the quantity of such parts amounts to a significant volume while the total parts replaced during the operational life of many vehicles is taken into account. Hence, ELV management is not confined only to end of life vehicles but proper management of consumable materials and replaced, serviced and spare parts from vehicle servicing and repair workshops also need to be managed properly to give totality to the ELV management issue.

2. State-of-the-art of ELV management

So much research have been conducted on ELV management, most of which basically deals with the management of vehicles that have arrived at their end of life stage. The automobile is the number one recycled product in America. Over 75% of the materials from cars are recycled. Recycled vehicles generate over 12 million tons of recycled steel, saving enough energy to power over 18 million homes for a full year [4]. According to the Retrievals Game [5], not only the economical assembly will be important in future cars, but so will be the economical disassembly, in which case many components will have to be designed in a completely new way. Furthermore, the work done in ELV management are also linked with establishing Extended Producer Responsibility (EPR) in vehicle manufacturing business [6] for having sustainable vehicle industry. The info is quite valuable to emphasize the importance of ELV management from green manufacturing aspect. The impacts have been depicted in the paper published by Environment Australia on Environmental Impact of End-of-Life Vehicles [1].

2.1 A Cradle to Incarnation

A concept called Cradle to Incarnation shown in fig.1[7], finds great significance when it comes to the issue of ELV management.

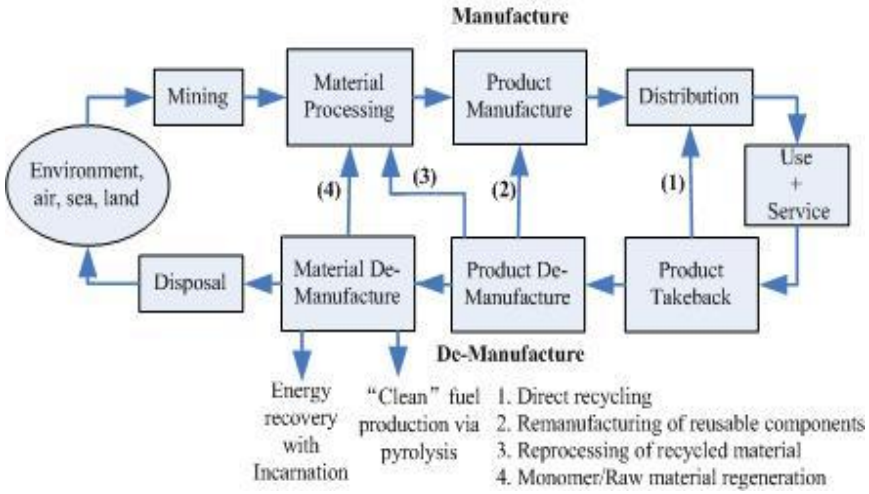


Fig. 1 Cradle to Reincarnation.

It is advisable that the vehicle life cycle also should follow the above loop "Cradle to Reincarnation" for proper management of ELV. If such loop can be followed in practice, then the resources consumed during the manufacturing of vehicles could be ultimately recovered from the ELVs, which is one of the basic thoughts of green manufacturing.

2.2 General description of existing ELV treatment process

Fig.2 below gives the general overview on ELV treatment process presently in practice [8]. The process begins after the stage of occurrence of end-of-life of the particular vehicle. Firstly, the fluids from the ELVs are drained or removed for recycling. And then the ELVs go through various dismantlement phases with the intension of recovering the parts and materials from the ELV.

Parts consisting of plastics such as the bumper and seats are usually recycled when needed, but mostly they remain behind and are compressed with the body, and the body is then subsequently transported to a shredder site. In the shredder plant a compressed ELV body is shredded and sorted into ferrous metal and non-ferrous material for material recovery. The shredder dust is dumped to landfill sites, sometimes after the incineration.

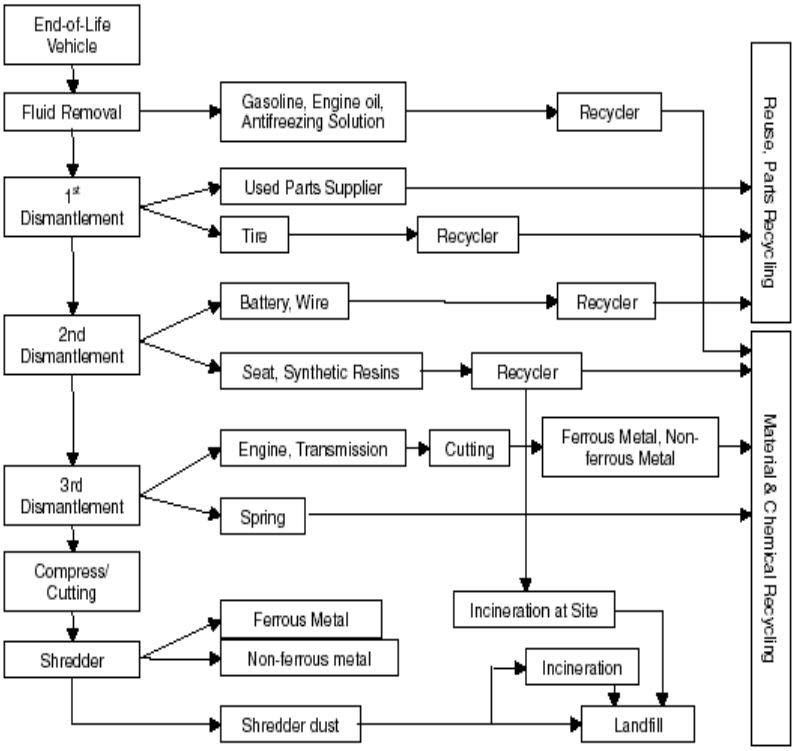


Fig. 2 Summarized flow sheet of ELV treatment system

3. A model for ELV management based on green manufacturing

"Green Manufacturing" is a modern manufacturing mode considering resources consumption and environmental impact, whose goal is to minimize the environmental impact and maximize the resources utilization during the whole product life cycle including design, manufacturing, packaging, transportation, use and disposal; meanwhile harmonizing the economic benefit of

enterprises and environmental benefit of the whole mankind. In the paper, a model for ELV management (ELVM) is proposed from this aspect of Green Manufacturing shown in fig. 3

The existing ELV management process seems to be dealing only with the vehicle unit remaining as a scrap unit at the end of the service life. However, it is not sufficient for the total ELV management task. The end-of-life vehicle management (ELVM) task will be complete only if the work is done from the very beginning stage of vehicle design prior to production and utilization and then finally turning down the out of use vehicle into an ELV. Additionally, the consumables and spare parts used and replaced during the vehicle maintenance and repair activity also need to be taken care of to give totality to the ELVM. The resources consumed by such spare parts is not negligible when the bulk volume of the vehicle units and parts are taken into account. The model propose for end-of-life vehicle management (ELVM) in the paper approaches the ELV management task from green manufacturing aspect and considers that management task for ELVM should begin at the very beginning stage of vehicle design followed by production, utilization & maintenance and then finally dumping & disposal of not useful vehicles i.e., ELV units. The bases of green manufacturing, namely; protection of environmental pollution and reduction of resources loss should be incorporated by the ELV management task.

Broadly, the proposed ELV management model employs two environmentally conscious aspects. The first is Environmentally Conscious Vehicle Design, Manufacturing and Utilization for ELVM. After the utilization the vehicle will arrive at its ELV stage. The second aspect is Environmentally Conscious Vehicle De-manufacturing and Disposal for ELVM whereby discarding and disposal of out of use vehicles takes place but it should be for the resource's recovery from such discarded vehicle units.

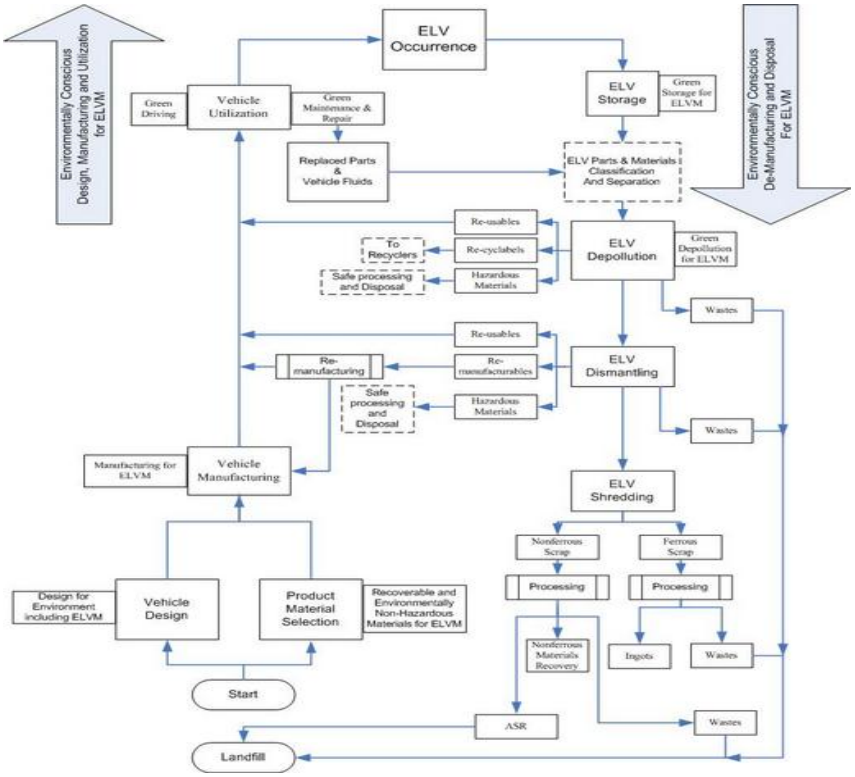


Fig. 3 A Model for ELV Management (ELVM) based on Green Manufacturing

3.1 ELV Management during Manufacturing and Utilization phase

This phase acknowledges that proper care should be taken during the design, production and utilization of the vehicle. The vehicle should be designed for the environmental friendly disposal and easy recovery of materials and parts from the ELV. Furthermore, the parts and materials replaced during the utilization of vehicles should be recovered and reused in vehicle manufacturing and utilization, thereby reducing the consumption of valuable resources.

3.1.1 Design for the environment including ELVM

The vehicle design should recognize the fact that like any other products, the vehicles also do have their certain lifespan. After the useful life is over, they need to be scrapped off and while doing so the design should consider the subject about materials and parts recovery at the end of vehicle's life. The design should not only reciprocate to the production and utilization issue of vehicle but also should reciprocate to the final disposal and materials recovery from the ELV. In other words, the vehicle should be designed for recoverable and green disposal. The design should not only deal with the economic assembly during the manufacturing but also should respond to economic dismantling of the vehicle at the end of their lives.

Traditionally issues considered in design are related only to function, appearance and financial concerns. As the decisions made by designers have a direct effect on the amount of raw material used, the amount of energy consumed and pollution produced by a product during its lifetime it is important that designers should use the right information and tools to minimize the effect their products will have on the environment. This is where the discipline of Design for the Environment (DFE) [10] has an important role to play and the following aspects should be covered by it.

- manufacture without producing hazardous waste
- use of clean technologies
- reduce product chemical emissions
- reduce product energy consumption
- use of non-hazardous recyclable materials
- use of recycled material and reused components
- design for ease of disassembly
- product reuse or recycling at end of life

3.1.2 Product Material Selection and use of toxic substances

Before starting the manufacturing process, the materials for production should be selected, keeping in mind the future impact of the materials in the environment. The cost of the materials that will decide the price of the vehicle is of course the major concern in order to compete in the market, but the selection of the materials should not be done looking at the cost aspect only, rather it is necessary to see the environmental impact it may cause in the future including the time when the vehicle arrives at the end of life stage.

The use of toxic substances like mercury should be avoided in the vehicle manufacturing [9]. Mercury-containing switches account for more than 99 percent of the mercury used in automobiles, with each switch containing approximately 0.8 grams of mercury. Automakers can prevent mercury emissions from retired vehicles if they employ clean production principles. This means designing vehicles to avoid the use of toxic substances like mercury in the first place and

accepting responsibility for the hazards due to their vehicles even after they are sold. Besides, a range of public and private policy initiatives must be started to reduce the threat from vehicle-related mercury pollution. Automakers can halt the proliferation of toxic contaminants in vehicles by utilizing “design for environment” approach that considers the life cycle environmental impacts in a product’s development. This should also include development of supplier specifications and material tracking systems to ensure that toxic substances are not used in auto manufacturing. Automakers can also voluntarily accept responsibility for hazards posed by their products at the end of their useful lives through product takebacks or by providing necessary guidelines in their technical manuals and assistance for the recovery system.

3.1.3 Manufacturing and Utilization for ELVM

Production should be optimized in terms of resource consumption and green manufacturing concepts should be implemented. The maximum use of recycled materials and the reusable parts from the ELVs will make production greener. The remanufacturing of the parts recovered from the ELVs and reuse of such parts in production of vehicles including in the maintenance and repair activity during the utilization of vehicles is quite important for ELVM based on green manufacturing.

During the utilization of the vehicle the proper care should be taken not only for the reliable utilization of the vehicle but also for the proper disposition of the vehicle at ELV stage. Improper maintenance will inhibit the recovery of parts and materials from the ELVs. The concept of green driving [11] is quite important to be implemented during the utilization phase. Proper care for the vehicle is a must. Regular maintenance and tune-ups, changing the oil and checking tire inflation can improve gas mileage, extend the vehicle's life and increase its resale value. It can also reduce traffic congestion due to preventable breakdowns, and it could reduce the vehicle's emissions by more than half. Giving long life to the vehicle by proper maintenance and driving method is also an affirmative aspect for ELVM since it will help to reduce the no of ELVs itself as the reliable vehicles will not be discarded by the users easily. This also, in a way, is prevention of resource losses.

3.2 ELV Management during De-manufacturing and disposal phase

After the state of occurrence of ELV, the ELVs need to be processed for disposal. Green processing and green disposal of ELVs are must for the purpose of environmental protection and minimization of resource losses. The existing ELV treatment practices, however, has dealt with the problem of ELV management after the occurrence of ELV to great extent. However, the paper intends to enlighten on followings to improvise the existing practice.

3.2.1 Green ELV storage

ELV storage should be such that it should not have any environmentally hazardous effect due to the keeping of ELV i.e., to say the ELV storage should be green. There should be a specified standard for the ELV storage facility, and it has been well defined by The End-of-Life Vehicles (Storage and Treatment) (Scotland) Regulations 2003 [12], which is as follows;

The keeping (even temporarily) of a waste motor vehicle prior to treatment shall only be carried out at a site -

(a) in appropriate areas, impermeable surfaces and provided with spillage collection facilities, decanters and cleanser-degreasers, and

(b) provided with equipment for the treatment of water (including rainwater) in compliance with all applicable legislation concerning health and environmental matters.

If the ELV storage is not proper, then the leakage of vehicle fluids to the ground or the contamination of vehicle parts and fluids with the rainwater will have unwanted effects on the environment. Thus, the ELV management should take account of well keeping of the ELVs.

3.2.2 ELV Depollution

Properly Stored ELVs should be moved to special depollution bays. These bays fitted with interceptor drainage systems to eliminate the possibility of ground contamination would be apposite from the view of green manufacturing. Firstly, the battery is to be removed and tested if it is suitable for use. If not send it to the battery recycler. All wheels and tires are then removed. The wheels can be reused depending on the physical condition and tires can be reused depending on the physical condition usually after re-soling, if not send to tire recycler.

A suitable vehicle drainage system is advisable that can safely remove hazardous liquids including engine oil, gearbox and transmission lubricants, fuel, coolant, windscreen wash, and brake and clutch fluids. It is better for oil filters to be removed and crushed to recover additional oils. These oils and recovered fluids should be recycled for future use according to their suitability.

Airbags and seat belt pretensioners are now routine on most cars. Strict precautions are required when removing these items and should have deployed them under controlled conditions.

Air conditioning systems are also common. These systems contain CFCs which destroy the ozone layer if not disposed of properly. All CFCs should be carefully removed and sent to specialists for further processing. Also, the vehicle parts containing toxic substances like mercury should be separated and subjected to safe disposal. For this the information about the toxic substances used in the vehicle is a must from the vehicle manufacturer without any secrecy for the benefit of environment.

3.2.3 ELV dismantling

After depollution, vehicles should be then moved to a dismantling bay where only the trained technicians should be used to remove useful parts. Many parts may get damaged during removal if unqualified technicians are allowed to perform and this is a loss from the view of green manufacturing since the opportunity for reuse and recovery of parts is eliminated which in fact is again the loss of valuable resources.

The removed parts should be labeled and shelved properly in the parts warehouse for easy retraction at the required time. If it is not possible to retract at the time of requirement then it is the wastage of resources again. Catalytic converters removed should be sent to specialists for recovery of the precious metal content. In addition, the parts and materials replaced during the vehicle maintenance and repair should also enter the stream of “parts and materials classification and separation” (shown in the proposed ELV management model block diagram) for the purpose of recovery and reuse same as that from ELVs.

The useful parts then recovered should be utilized to repair and maintain the other vehicles currently in operation. Many times, the parts like alternators and starter motors can be used as good as the new ones after proper reconditioning. Other times the remanufacturing of parts will be necessary to enable the reuse. Hence, the ELV management should intend to maximize the

use of such parts and materials either during vehicle production or during vehicle utilization (mainly maintenance and repair activity).

Many times, it so happens that the vehicles are left as ELVs after an accident occurs. In case of not major accidents, many parts of the vehicles will be in good working condition including the engine of the vehicle. In such cases, the whole engine assembly can be removed and after rigorous testing with the use of dynamometers such engine can be replaced in another similar model vehicle. Furthermore, many automakers nowadays are starting up engine remanufacturing business which can be regarded as a plus point while viewed from the angle of green manufacturing for the task of ELV management.

Theoretically, the entire contents of an ELV could be removed for reuse in one form or another in another vehicle. Realistically, however, logistical and economic reasons limit removal operations. Listed below are typical parts/materials removed and their typical ultimate disposition.

- Electro-mechanical parts (clutches, water pumps, engines, starters, alternators, transmissions and motors for power windows including mechanical parts like engine blocks, crankshafts, camshafts, engine heads, differentials, torque converters): Typically remanufactured and reused.
- Structural body parts (body panels, wheels, etc): Removal for use in repairing accident damaged vehicles.
- Aluminum and copper parts: Removal for sale directly to nonferrous processors. Alternatively, dismantlers can make ingots from the parts and sell them to the nonferrous scrap market.
- Gasoline: Recovered for use.
- Vehicle fluids (engine oil, transmission fluid, ethylene glycol, windshield cleaning fluid): Recycled.
- Batteries: Used if in good condition or sent to a lead-acid battery recycler for recycling.
- Tires: Sent to a scrap tire dealer for disposition (typically burned for energy recovery, landfilled or stockpiled)
- Catalytic converters: Sent to a recycler for precious metal (platinum) recovery
- Air conditioning refrigerant gases: Recovered for reuse or destruction.
- Air bags: Recovered for reuse or deployed and disposed of.
- Fuel tanks: Steel tanks are flattened and recycled; plastic tanks are disposed of in landfills.

3.2.4 Shredding and Post shredder material processing:

What remains of the vehicle after dismantlers has removed all useful parts and materials (commonly referred as the “hulk”) typically consist of steel structural materials, plastic dashboards, foam seats, and other components. The hulk is typically flattened for ease of transport to the shredder. Following the dismantling process, gutted ELVs are to be sent (typically flattened) to a shredder for shredding. After the shredding of hulk, the post shredder task is separation of shredded materials into two basic streams i) ferrous metal and ii) nonferrous materials.

Following shredding, two basic separations are to be made:

- An initial separation of the combined material stream into ferrous and nonferrous fractions using a magnetic separation process.
- Separation of the nonferrous material stream into metal and non-metal fractions using a variety of techniques (typically air separation performed at the shredder).

The three basic streams thus generated are:

- Ferrous metal (iron and steel)
- Non-ferrous metal (aluminum, stainless steel, copper, brass, lead, magnesium, zinc, and nickel)
- Shredder dust or Auto Shredder Residue (ASR) (consisting of materials like plastics, glass, rubber, foam, carpeting, textiles, etc.)

The separated ferrous metal fraction (containing iron and steel) is to be sent for recycling to steel smelters. The separated non-ferrous metal fraction (containing aluminum, brass, bronze, copper, lead, magnesium, nickel, stainless steel, and zinc) is to be sent to another specialized facility to separate the stream into its individual metals. The ASR generated contains the bulk of non-metallic materials present in shredder hulks (plastics, glass, rubber, foam, carpeting, textiles, etc), entrained metallic fines, dirt and moisture. ASR can be further divided into two streams namely;

- "Light" ASR ("fluff"): Generated at the shredder facility when the nonferrous fraction is separated into metal and nonmetallic streams using air classification processes (the nonmetallic fraction being "fluff").
- "Heavy" ASR: Generated at the non-ferrous metal processing facility during separation of the various metal steams (the heavy ASR representing rejected contaminants extracted during processing).

In general, both light and heavy ASRs are landfilled. Further, research should be done for the management of ASR so as to recover more materials from the ELVs and reduce the wastes going to the landfill.

3.2.5 Circular Economy and End-of-Life Vehicle (ELV) Management:

A circular economy aims to move away from the conventional linear model of *"take–make–use–dispose"* by keeping products, components and materials in productive use for as long as possible. In the automotive sector, End-of-Life Vehicle (ELV) management is an important part of this transition because vehicles contain substantial quantities of steel, aluminium, copper, plastics, rubber, glass, batteries and other valuable materials. A circular approach prioritizes prevention, reuse, repair, remanufacturing, component recovery and high-quality recycling, while minimizing disposal and environmental pollution. It also begins at the vehicle-design stage through design for dismantling, repairability, recyclability and recoverability. The European Union's current ELV framework explicitly follows this lifecycle approach, covering vehicle design and production through collection, dismantling, reuse and recycling, with greater emphasis on recovering valuable and critical raw materials [13].

Effective ELV management therefore creates a closed-loop material system in which recovered components and materials from old vehicles become inputs for new vehicles and other industrial products. The process normally involves collection, depollution, dismantling, testing and reuse of suitable parts, followed by material separation, shredding and recovery of metals and other recyclable materials. The EU's earlier End-of-Life Vehicles Directive 2000/53/EC established

targets of at least 95% reuse and recovery and 85% reuse and recycling by average vehicle weight, demonstrating the importance of measurable recovery targets in a circular automotive system [14]. The newer EU ELV Regulation, which entered into force in August 2026, further strengthens circularity through requirements for vehicle design, recycled content, improved traceability, producer responsibility and higher-quality material recovery [15]. Thus, ELV management should be viewed not merely as vehicle waste disposal, but as a strategic resource-recovery system that can reduce demand for virgin raw materials, conserve energy and materials, create recycling and remanufacturing industries, and reduce the environmental impacts associated with discarded vehicles.

4. Conclusion

The paper concludes by making a well-recognized remark that ELV management is an important aspect for environmental protection with the views of preventing pollution and minimizing resource losses, which are the bases of green manufacturing. With the increase in the number of vehicles on road, the numbers of vehicles arriving at their end of life are also in increase and needs to be well managed. The ELV management model presented in the paper mainly focuses on the following issues to give totality to the ELV management task.

1) Design of vehicles and selection of the product materials should respond to the ELV management.

2) Production and Utilization of the vehicles should minimize the resource consumption by implementing green manufacturing and utilizing the recyclable and reusable parts and materials from the ELVs.

3) ELV storage should be green in terms of environmental friendliness with no detrimental effect from the stored ELVs.

4) ELV depollution, dismantling and shredding steps should be for the resource recovery from the ELVs so as to utilize the recovered resources in vehicle manufacturing and maintenance activity, if not simply for the resource recovery by various material processing processes.

5) The parts and materials replaced during the vehicle maintenance and repair activity should be made to enter the stream of ELV management model for the recovery of the resources from such parts and materials.

Acknowledgments

Chongqing University, Institute of Manufacturing Engineering and Chongqing Municipality.

Funding

China Scholarship Council with Chongqing University Scholarship.

Conflict of Interest

The author(s) declared no conflict of interest.

Data Availability

The proposed model is available and can be accessed, subject to ethical, legal, institutional, or confidentiality restrictions.

References:

[1] Environmental Impact of End-of-Life Vehicles: An Information Paper Environment Australia, A publication of the Commonwealth Department of Environment and Heritage ©2002, ISBN 0642547513

[2] 中国汽车产品回收利用技术政策研究 2003 年 11 月 [The Policy of Study for Recycling Technology for Chinese Automotive Products (Final Report)]

[3] Directive 2000/53/EC of the European Parliament and of the council of 18 September 2000 on end of life vehicles, 2000. Official Journal of the European Communities L269, 21-10-2000

[4] 2004 Pit Stops Fact Sheets Connecticut Department of Environmental Protection, 79 Elm Street, Hartford, CT 06106-5127 Office of Pollution Prevention (860) 424-3297 www.dep.state.ct.us/wst/p2/vehicle/abindex.htm Fact Sheet: DEP-P2-PITSTOPS-FS-010 Last Updated: August, 2004

[5] Green design in the automobile industry, Leigh Holloway, Sheffield Hallam University, David Walker, Open University

http//www.co-design.co.uk/green.htm

[6] Green Cars, End-of-Life Vehicle Management: Product Tack-Back, An Implementation Tool for EPR Principles http://www.environmentaldefense.org/documents/894_GC%5Ftakeback%2Ehtm

[7] Klaus Bellmann , Anshuman Khare. Economic issues in recycling end-of-life vehicles. Technovation 20 (2000) 677–690

[8] Ki-Heon Kim a, Hyun-Tae Joung etc. Management status of end-of-life vehicles and characteristics of automobile shredder residues in Korea. Waste Management 24 (2004) 533–540

[9] TOXICS IN VEHICLES: MERCURY. Implications for Recycling and Disposal. EXECUTIVE SUMMARY. January 2001 http://www.cleancarcampaign.org/pdfs/execsumm

[10] Tracy Dowie-Bhamra. Design for Disassembly. Green Design. University of Manchester. http://www.co-design.co.uk/design.htm#ret19

[11] Top Ten Tips for Green Driving. American Lung Association. April 2000.

http://www.lungusa.org/site/pp.asp?c=dvLUK9O0E&b=36090

[12] Scottish Statutory Instrument 2003 No. 593. The End-of-Life Vehicles (Storage and Treatment) (Scotland) Regulations 2003

[13] End-of-life Vehicles-Environment-European Commission https://environment.ec.europa.eu/topics/waste-and-recycling/end-life vehicles

[14] Eur-Lex Directive 2000/53/EC

https://eur-lex.europa.eu/legal-content/EN/TXT/?uri=CELEX%3A32000L0053

[15] End-of-life Vehicles-Environment-European Commission https://environment.ec.europa.eu/topics/waste-and-recycling/end-life-vehicles/end-life-vehicles-regulation

TECHNO-ECONOMIC ANALYSIS OF GRID-CONNECTED SOLAR PV-BESS SYSTEM FOR A MANUFACTURING INDUSTRY: A CASE STUDY OF ASIAN BISCUITS AND CONFECTIONERY, SUNSARI, NEPAL

Nirmal Kumar Subeed[1*], Nawraj Bhattarai[2],

[1*]Department of Mechanical and Aerospace Engineering/ Pulchowk Campus/ Institute of Engineering / Tribhuwan University
Lalitpur, Nepal
079msree013.nirmal@pcampus.edu.np

[2]Department of Mechanical and Aerospace Engineering/ Pulchowk Campus/ Institute of Engineering / Tribhuwan University
Lalitpur, Nepal
bnawraj@ioe.edu.np

Abstract

Behind the meter adoption of solar Photovoltaic (PV) systems in the industrial sector is increasing due to their potential to reduce electricity costs and carbon emissions. However, the intermittent nature of solar PV and the requirement for reliable power supply creates a need for Battery Energy Storage Systems (BESS). In Nepal, where electricity generation is predominantly hydropower based, PV-BESS integration in industrial facilities remains less explored. This study presents a techno-economic analysis of a grid connected solar PV-BESS system for a manufacturing industry in Sunsari, Nepal. A two-stage modelling approach was adopted. First, the PV system was designed and simulated using PVsyst, followed by BESS optimization using HOMER Grid. A 600 kWp solar PV system with a 2450 kWh BESS resulted in the lowest Net Present Cost (NPC), with an overall system Levelized Cost of Electricity (LCOE) of USD 0.054/kWh. Financial analysis showed that allocating 30% of the BESS capacity for Diesel Generator (DG) replacement and 70% for peak shaving resulted in an NPV of USD 30,967.45, an IRR of 8.67%, and a payback period of 7.89 years. Changing the allocation to 20% DG replacement and 80% peak shaving reduced the IRR to 6.43% and increased the payback period to 11.32 years making BESS allocation among the most sensitive parameter. The optimized PV-BESS system could reduce approximately 308.15 tCO_2-eq annually. The findings indicate that PV-BESS integration can reduce electricity costs and enhance energy resilience when BESS is strategically allocated according to site specific load, tariffs and grid outage characteristics.

Keywords: Solar Photovoltaic, Battery Energy Storage System, Techno-economic analysis, PV Syst simulation, HOMER Grid optimization

1 Introduction

1.1 Background

The rapid growth in electricity demand and the need to reduce Carbon Dioxide (CO_2) emissions have accelerated the deployment of renewable energy technologies worldwide. Solar Photovoltaic (PV) has become one of the fastest-growing sources of electricity generation, while Battery Energy Storage System (BESS) are increasingly being adopted to improve the flexibility, reliability, and utilization of variable renewable generation (International Energy Agency, 2026).

The transition towards renewable energy is also reflected in Nepal's energy sector, where increasing attention has been given to diversifying the energy mix and promoting renewable energy technologies.

Solar PV has particular potential for distributed electricity generation because it can be installed close to electricity consumers without requiring large areas of land. This characteristic is especially relevant for industrial facilities, where unused rooftop areas can be utilized for electricity generation without competing directly with agricultural or other productive land uses.

The adoption of rooftop solar PV systems in Nepal's industrial sector has increased significantly in recent years. By early 2026, approximately 40 Mega Watts (MW) of rooftop solar capacity had been installed, while the pipeline of projects exceeded 100 MW, indicating a substantial expansion of interest in rooftop solar among industries and Small and Medium Enterprises (SMEs) in Nepal (Alternative Energy Promotion, 2026).

1.2 Problem Statement

Despite this increasing penetration, conventional grid-connected solar PV systems remain highly dependent on the availability of the utility grid for their operation. During grid interruptions, these systems are generally incapable of supplying power independently and can continue operating only in the presence of Diesel Generator (DG) operation (Mansour Alramlawi et al., 2018). Industrial loads may extend beyond solar production hours, while electricity tariffs may vary according to time of use. In such circumstances, BESS can provide additional value by shifting solar energy to higher-value periods, reducing grid electricity consumption during peak-tariff periods and supporting critical loads during grid interruptions. BESS can also reduce the operating requirement of DGs, which are commonly used as backup sources during grid outages.

The economic value of BESS, however, is highly dependent on site-specific load characteristics, tariff structure, outage frequency and duration, PV generation profile, battery cost and system operating strategy. In Nepalese industries, irregular and unpredictable duration of grid interruptions may not justify sizing BESS solely for backup purposes because the storage asset may remain underutilized during normal operation. Therefore, an economically appropriate BESS should ideally provide multiple services, including solar energy shifting, peak-load management and backup support during grid interruptions.

1.3 Novelty and Objectives of the Study

The principal contribution of this study is the integration of industrial operating load data, site-specific PVsyst simulation and Hybrid Optimization Model for Electric Renewables (HOMER) grid-based BESS optimization for a Nepalese food manufacturing facility. The BESS is assessed for multiple applications, including solar-energy utilization, peak-load management and reducing DG dependence during grid interruptions.

The main objective of the study is to conduct a techno-economic assessment of a grid-connected rooftop Solar PV-BESS system for a manufacturing industry.

The specific objectives are to:

i) To perform the technical feasibility and energy yield of the rooftop PV system

ii) To determine optimal PV-BESS sizing along with system configuration.

iii) To evaluate the economic performance of the optimized solar PV-BESS system and perform sensitivity analysis.

iv) To identify net CO2-eq emission reduction from the optimized PV-BESS system.

The remainder of the paper is organized as follows. Section 2 presents the literature reviews of similar past research studies. Section 3 presents the materials and methods, including the study area, data collection, rooftop PV design, PVsyst simulation, HOMER Grid optimization. Section 3 and section 4 presents results and discussion respectively whereas section 6 and section 7 presents the limitation and conclusion respectively.

2 Literature Review

Previous studies have investigated the techno-economic feasibility of grid-connected solar PV systems integrated with BESS, particularly for reducing electricity costs, managing peak demand, and improving renewable energy utilization. Chih-Ta Tsai et al., (2020) examined BESS sizing for an industrial behind-the-meter consumer in Taiwan and demonstrated that battery storage can reduce electricity expenditure and peak demand under appropriate Time-of-Use (TOU) tariff structures. Similarly, Cheng-Yu Peng et al., (2021) investigated PV-BESS sizing and tariff optimization for an industrial application in Taiwan, highlighting the importance of appropriate system sizing in reducing electricity costs and improving PV utilization. These studies indicate that the economic value of BESS depends not only on installed capacity but also on the interaction between electricity demand, tariff structures, and battery dispatch strategies.

The influence of electricity tariffs, battery degradation, and system costs on project feasibility has also been widely investigated. Sepúlveda-Mora et al., (2021) demonstrated that TOU tariffs can improve the economic attractiveness of PV-BESS systems in commercial buildings, while battery degradation and replacement assumptions substantially influence lifecycle costs. Han et al., (2022), through techno-economic optimization for different consumer groups in Switzerland, similarly found that economic performance is sensitive to electricity prices, load profiles, investment costs and future tariff developments. More recent industrial research by Matera et al., (2025) further examined the performance of an integrated PV-BESS system using hourly simulation over a 30-year period. Collectively, these studies suggest that PV-BESS integration does not necessarily improve economic performance in every application. Its feasibility depends on the characteristics of the consumer, the operating strategy and the underlying financial assumptions.

Studies from South Asia provide additional insights into the application of PV-BESS systems under regional operating conditions. Regmi et al., (2022) evaluated a grid-connected PV-DG hybrid system with and without battery storage in Nepal, reporting improved techno-economic performance and reduced dependence on diesel for the PV-BESS-DG configuration. In India, Boruah & Chandel, (2024) combined detailed PV system simulation using PVsyst with HOMER grid-based optimization and economic analysis, demonstrating the usefulness of an integrated modeling approach for assessing system feasibility. Other studies, including Hopley et al., (2024) and Jivaganont & Mongkoltanatas, (2021), have emphasized that battery storage is not automatically economically beneficial and that its profitability depends on industrial load characteristics, battery costs, TOU tariffs, and degradation. Although these studies provide valuable methodological and practical insights, their findings are associated with specific consumer profiles, tariff structures, and economic conditions, limiting their direct applicability to other industrial settings.

Despite these advances, a case-specific assessment is necessary to determine the appropriate PV and BESS capacities and operating strategies for energy-intensive industries in Nepal. In

particular, the combined influence of industrial load characteristics, Nepal's TOU tariff structure, grid electricity consumption, DGs operation and battery dispatch on the technical and economic performance of PV-BESS systems requires further investigation. The present study addresses this need through a techno-economic assessment of a grid-connected PV-BESS system for Asian Biscuits and Confectionery in Sunsari, Nepal. It employs a two-stage modeling approach, using PVsyst for PV system design and energy yield estimation and HOMER Grid for system optimization and economic evaluation. The analysis incorporates an industrial load profile developed from electricity consumption data and evaluates the integration of PV, BESS, grid electricity, and DGs backup under the applicable operating and financial assumptions. By examining battery sizing, peak shaving, DGs displacement and key economic indicators, the study aims to provide an industry-specific assessment of PV-BESS feasibility and identify the conditions under which battery storage can improve industrial energy performance in Nepal.

3 Materials and Methods

3.1 Research Methodology Flowchart

The methodological flowchart carried out to perform the research is shown in Figure 1.



Figure 1:Research Methodological Flowchart

3.2 Study Area and Data Collection

This study investigated the techno-economic and environmental performance of a grid-connected solar PV-BESS at Asian Biscuits and Confectionery Pvt. Ltd., a food manufacturing industry in Sunsari District, Koshi Province, Nepal (Latitude: 26°35′16.5″N, Longitude: 87°16′28.7″E). Figure 2 shows the exact pin point location of the selected study area in the Koshi province map of Nepal.

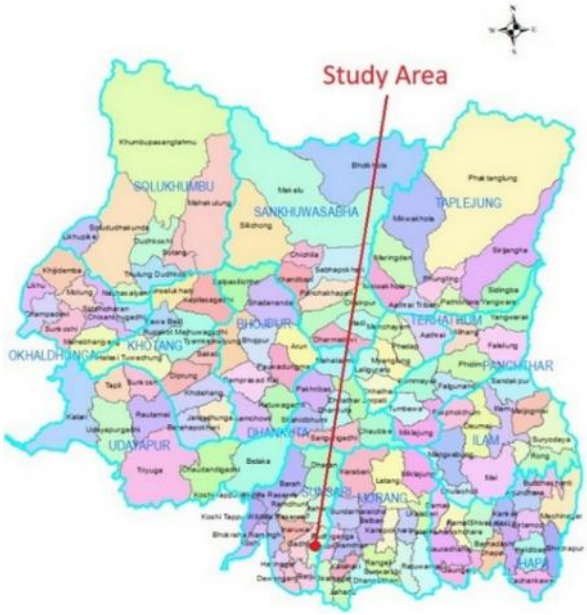


Figure 2: Study area location marked in Koshi province map of Nepal(Government of Nepal, n.d.)

The facility is supplied by the NEA grid, with DGs providing backup during grid outages. The industry has an approved load of 750 kVA, a 1000 kVA transformer and two existing DGs rated at 600 kVA and 373 kVA.

Figure 3 shows the twelve months of NEA electricity consumption records for FY 2081/82 and Figure 5 shows collected one month of hourly electricity data from the grid meter. The monthly consumption data established the annual energy demand, while the measured hourly data characterized the temporal load distribution. An annual 8,760-hour load profile was reconstructed using a data-driven mathematical method (Mario Lamagna et al., 2020). NEA reported outage frequency and repair time data for Koshi Province were used to characterize grid interruptions, supplemented by the industry's DG operating data and critical load requirements as shown in Figure 4.

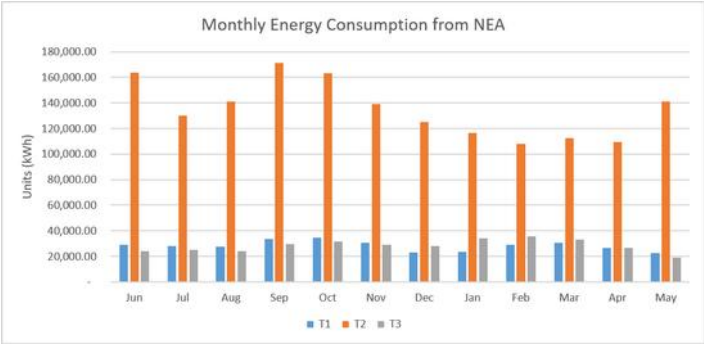


Figure 3: Monthly Energy Consumption from NEA by the industry in FY2081-2082

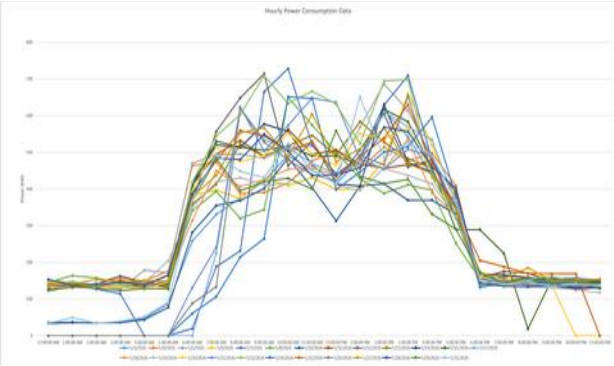


Figure 5: Hourly load data of the industry for a month

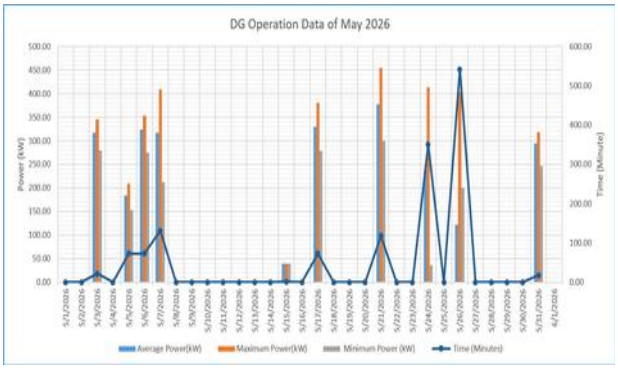


Figure 4: DG operation data of the industry for a month

3.3 PV System Design, Technology Selection and Energy Simulation

The rooftop PV system was designed considering the available roof area, site-specific solar resources, industrial electricity demand and the applicable grid-interconnection limit. Although the theoretical energy-based PV requirement was approximately 1670 kWp, the allowable maximum permissible AC capacity under the applicable NEA net-metering provision limited the inverter capacity to 500 kW. Accordingly, a DC/AC ratio of 1.20 was adopted, resulting in a 600 kWp DC PV array and 500 kW AC inverter capacity. The roof spaces assessment carried out to identify the available roof spaces for solar PV installation is shown in the Figure 6.

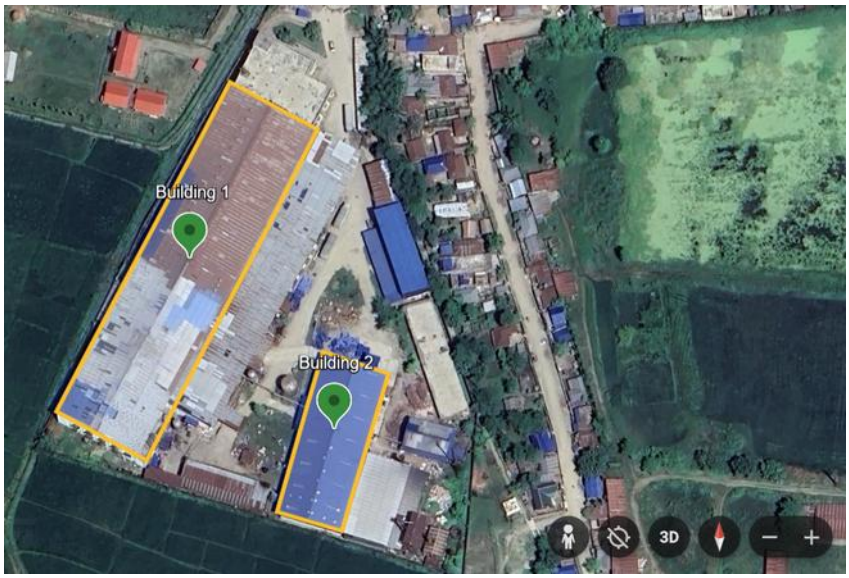


Figure 6: Google Earth Image of the Industry roofs suitable for solar PV installation

The detail technical configuration of the system is shown in the Table 1.

Table 1: Technical configuration of solar PV system

Component	**Specification**
Solar Module	625Wp Per Module
Total No. of Modules	960 Nos.
Total System Capacity	600 kWp -DC 500kW -AC

Inverters	4 Nos. of 125kW Each	
MPPT per Inverter	12 MPPTs	
Strings per MPPT	2 Strings per MPPT	
Strings per Inverter	17 Strings	
Modules per String	Type:1	Modules in Series: 14 Nos. Modules in Parallel: 1 Nos.
	Type:2	Modules in Series: 16 Nos. Modules in Parallel: 1 Nos.

For the grid connected solar PV system, the selected technologies technical specifications are detailed in Table 2 and Table 3 for solar PV module and string inverter respectively.

Table 2: Technical Specifications of Solar PV

S.N.	**Parameters**	**Units**	**Values**
1	Model Number	JAM66D45-625/LB	
Electrical Characteristics			
2	Peak Power Watts-P_{max}	W_p	625
3	Power Tolerance- P_{max}	W	0+3%
4	Maximum Power Voltage-V_{MPP}	V	40.45
5	Maximum Power Current-I_{MPP}	A	15.45
6	Open Circuit Voltage-V_{OC}	V	48.70
7	Short Circuit Current-I_{SC}	A	16.15
8	Module Efficiency	%	23.1
Mechanical Characteristics			
9	Solar Cells	-	Monocrystalline
10	No. of Cells	Cells	132 (6 x 22)
11	Module Dimensions	mm	2382 x 1134 x 30
12	Weight	kg	33.1

Table 3: Technical specification of string inverter

S.N.	**Parameters**	**Units**	**Values**
1	Model Number	SG125CX-P2	
Input Parameters			
2	Max. Input Voltage	V	1100V
3	Max. PV input current	A	360
4	Max. Short Circuit Current	A	480
5	Start Voltage	V	200
6	MPPT Operating Voltage Range	V	180-1000
7	Rated PV Input Voltage	V	600V
8	No. of MPPT Trackers	Nos.	12
Output Parameters			
9	Max. AC Active Power	W	125
10	Max. AC Apparent Power	kVA	125
11	Max. AC Active Current	A	181.1
12	AC Voltage Range	V	320-480
13	Rated Grid Frequency	Hz	50/60
14	Nominal Output Current	A	181.1
15	Adjustable Power Factor Range		0.8 Leading – 0.8 Lagging
16	Max. Total Harmonic Distortion		<3%
Efficiency			
17	Max. Efficiency	%	98.5

PV energy production was simulated using PVsyst 8.0.6, with module tilt and azimuth aligned with the existing roof orientation and site-specific meteorological data obtained from Meteonorm 8.2. The resulting hourly PV generation profile was subsequently used as an input to the system optimization model. Figure 7 shows the 3D scene defined in PV syst for shadow analysis of the designed PV system.

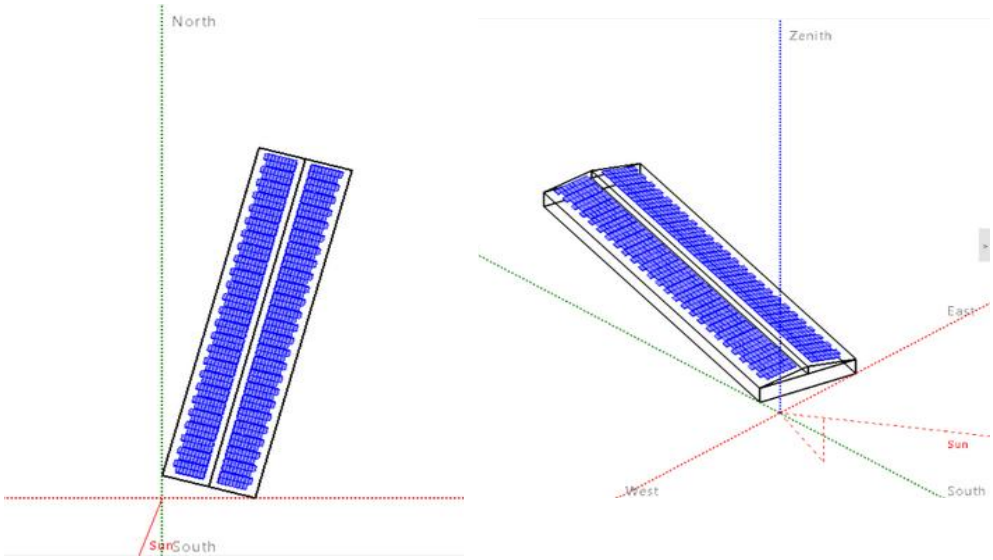


Figure 7: Shading Analysis performed in PV Syst

3.4 PV-BESS System Modelling and Optimization

HOMER Grid software was used to optimize the BESS capacity and operating configuration while retaining the PV system at its predefined capacity of 600 kWp DC and 500 kW AC. The model incorporated the reconstructed hourly load profile, hourly PV generation, NEA time-of-day electricity tariffs, grid availability, existing DG characteristics, battery technical parameters and economic assumptions. The grid and existing DG were retained as available electricity sources.

The primary optimization objective was to minimize the total net present cost (NPC) of the overall system configuration over the project lifetime. BESS energy capacity (kWh) and power rating (kW) were the decision variables. The optimization considered the hourly balance between PV generation, grid supply, DG output, industrial demand, battery charging and discharging and surplus-energy curtailment. Battery operation was assessed for peak shaving and DG replacement during grid interruptions. Figure 8 shows the HOMER analysis architectural process diagram.

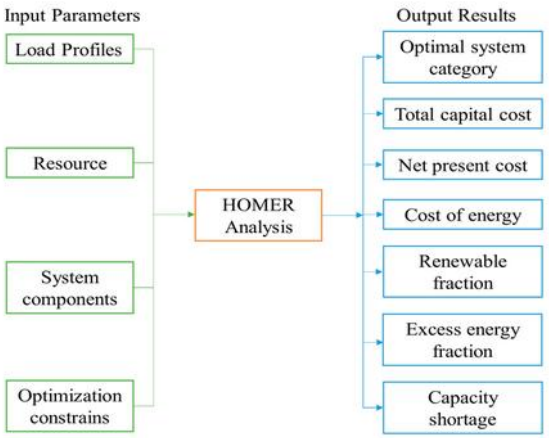


Figure 8:HOMER software simulation analysis process architecture diagram

3.5 Economic and Sensitivity Analysis

The economic assessment considered capital expenditure, operation and maintenance (O&M) costs, electricity-bill savings, financing assumptions, and project lifetime. Capital costs were primarily obtained from quotations provided by local engineering, procurement, and construction (EPC) companies and battery vendors. Costs quoted in Nepalese rupees (NPR) were converted to US dollars (USD) using the Nepal Rastra Bank selling exchange rate of NPR 152.23/USD dated 7 August 2026.

The project lifetime was assumed to be 25 years, based on the expected service life of the solar PV modules. The LFP BESS replacement cost was excluded from the economic analysis. The principal economic assumptions included a discount rate of 8%, inflation rate of 5%, debt-to-equity ratio of 80:20, debt interest rate of 8%, loan repayment period of seven years, and annual O&M costs equivalent to 0.75% of the total project cost. The economic performance was evaluated using net present value (NPV), internal rate of return (IRR), and simple payback period.

The capital cost breakdown for the proposed solar PV–BESS system, based on the collected vendor quotations, is presented in Table 2.

Table 4: Capital Expenditure cost for the solar PV-BESS

S.N.	Component	Quantity	UoM	Amount (USD)	Pricing Source
1	Solar PV System	600	kWp	94,594.00	Quotation from local EPC company
2	On Grid String Inverter	500	kW	26,276.00	Quotation from local EPC company
3	Balance of the System	600	kWp	64,324.00	Quotation from local EPC company
4	System Engineering, Desing and Installation	600	kWp	8,909.00	Quotation from local EPC company
5	Contingency	1	Lot.	2,970.00	Quotation from local EPC company
6	BESS	2450	kWh	5,11,560.00	Quotation form Vendors including transportation.
Total Cost				7,08,633.00	

Sensitivity analysis evaluated the effects of changes in project cost, BESS allocation for DG replacement and peak shaving, PV energy generation, NEA electricity tariffs, interest rate, and discount rate. Each parameter was varied individually while the other parameters were held constant, and the resulting changes in IRR and payback period were compared with the base case.

3.6 CO2-Equivalent Emission Assessment

The environmental assessment estimated annual CO_2-equivalent emission changes associated with the proposed PV–BESS system relative to the existing electricity-supply arrangement. Emissions were calculated from the electricity supplied by each source and its corresponding emission factor:

The annual CO_2 emissions associated with electricity consumption were estimated using equation (1).

(1)

Where, is the annual CO_2-eq emissions (kg CO_2/year), is the electricity supplied from the corresponding source (kWh/year) and EF is the emission factor of the respective energy source (kg CO_2/kWh).

The assessment considered avoided grid-electricity emissions through PV generation, avoided DG emissions through battery discharge, and emissions associated with grid electricity used for battery charging and the lifecycle impacts of the PV and LFP battery systems. The resulting avoided and additional emissions were combined to estimate the net annual CO_2-equivalent emission reduction.

4 Results

4.1 Industrial Load Reconstruction and PV Performance

The reconstructed annual hourly load profile showed good agreement with measured data, achieving a Normalized Mean Bias Error (NMBE) of 2.34% and a coefficient of variation of the Root Mean Square Error (cvRMSE) of 10.16%. These results indicate satisfactory accuracy for subsequent energy-system modelling. The reconstructed 8760-hour load data of the industry imported in the HOMER grid is shown in the heatmap diagram in Figure 9.

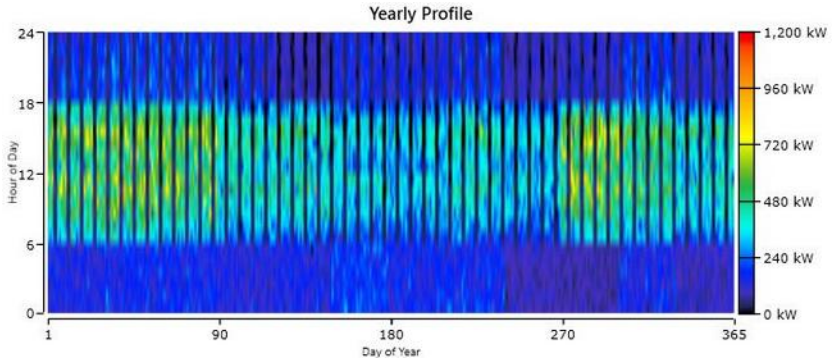


Figure 9: Heatmap showing the reconstructed hourly load profile of the industry imported into HOMER Grid

The proposed 600 kWp rooftop PV system was simulated in PVsyst and the approximate simulated annual energy generation is 782 MWh. Monthly generation ranged from 45.98 MWh in January to 84.74 MWh in May, reflecting seasonal variations in solar availability. The monthly performance ratio (PR) remained between approximately 0.83 and 0.88, with the highest value in February and the lowest in May. Figure 10 shows the PV system energy production at different probability and the system monthly PR.

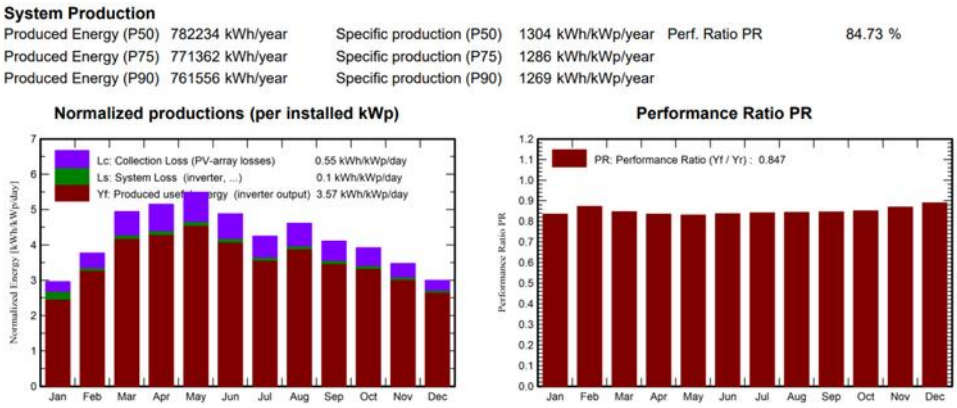


Figure 10: Monthly normalized energy production and system monthly performance ratio

The highest PR of approximately 0.88 was observed in February, while the lowest value of approximately 0.83 occurred in May as shown in Figure 11. The results indicate that higher solar irradiation increases the available solar energy and, consequently, the absolute PV energy output; however, the increase in ambient and module operating temperature during periods of high irradiation can increase thermal losses and reduce the conversion efficiency of the PV modules. Therefore, the month with the highest energy generation does not necessarily correspond to the highest performance ratio.

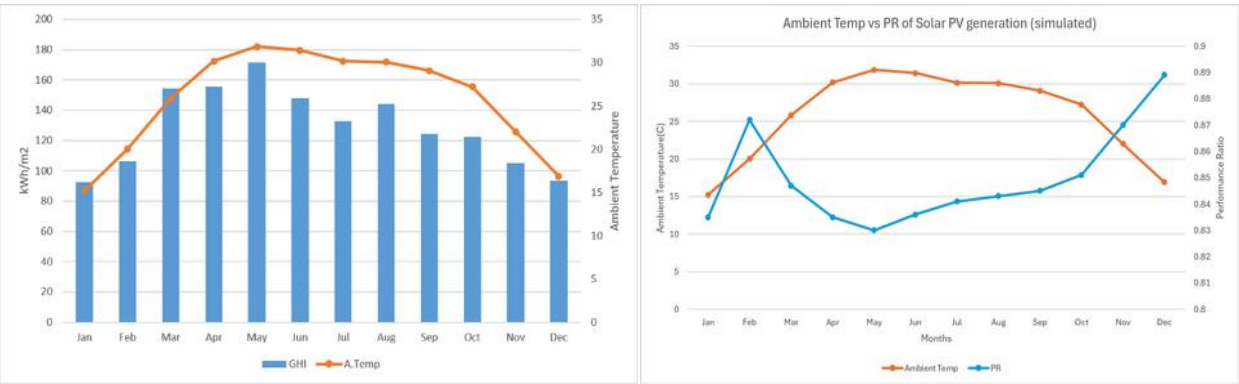


Figure 11:a) Global Horizontal Irradiance vs Ambient Temperature (b) Ambient Temperature vs Performance Ratio Analysis

4.2 Optimal PV-BESS Configuration and Operating Performance

HOMER Grid identified the combination of 600 kWp PV, BESS of 2450 kWh with 600kW power output, utility grid and existing DG as the optimal configuration. It achieved the lowest NPC of approximately USD 2.92 million and a LCOE of USD 0.054/kWh among the three

leading feasible configurations. The Figure 12 shows the economic comparison of the optimal system configuration achieved from the HOMER grid result.

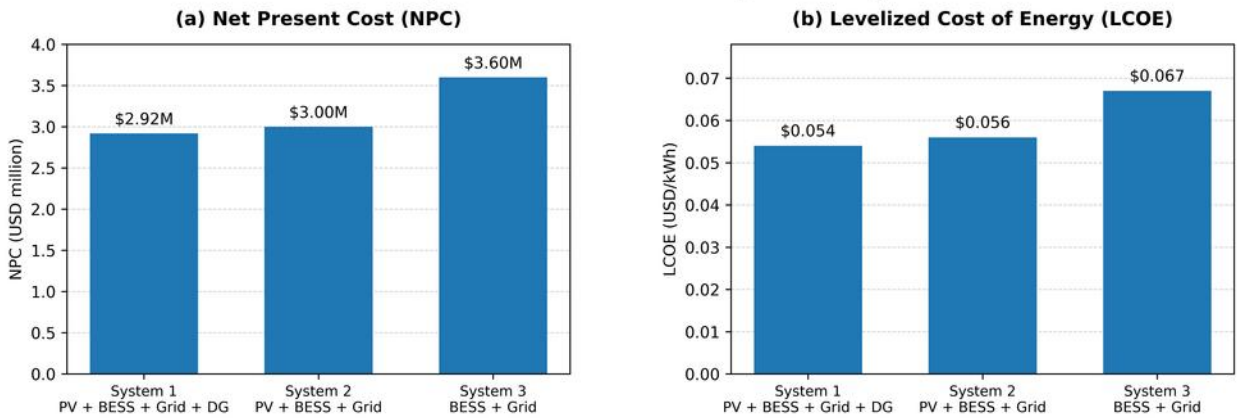


Figure 12: Economic comparison of HOMER grid optimized systems

4.3 Economic and Sensitivity Analysis

The PV-BESS from the optimal system configuration achieved from HOMER grid required an initial capital investment of USD 708,924, comprising USD 197,364 for PV and USD 511,560 for BESS. The existing DG was included without additional capital cost in the optimization. The HOMER optimized system configuration provides an average annual utility-bill saving of approximately USD 43,610, with an LCOE of USD 0.054/kWh and a NPC of USD 2.92 million, indicating favorable economic performance compared with the other feasible configurations.

A separate financial analysis was performed for the PV-BESS investment. The analysis resulted in an IRR of 8.67%, NPV of USD 30,967.45, and a payback period of 7.89 years. These results indicate that the financial viability of the PV-BESS investment depends not only on the initial investment cost but also on its effective utilization for reducing grid electricity purchases and supporting the industrial load during periods of high demand and grid outages.

Sensitivity analysis identified BESS allocation for DG replacement as the most influential parameter affecting financial performance. Reducing the allocation from 30% to 20% decreased the reported IRR from 8.67% to 6.43% and increased the payback period from 7.89 to 11.32 years. Increasing the allocation to 40% improved the IRR to 10.88% and shortened the payback period to 6.87 years. Project cost was the second most influential parameter, whereas interest-rate variations had comparatively limited effects within the ranges assessed.

Figure 13 and Figure 14 shows the tornado chart of the influential parameters on the project IRR and project payback period respectively.

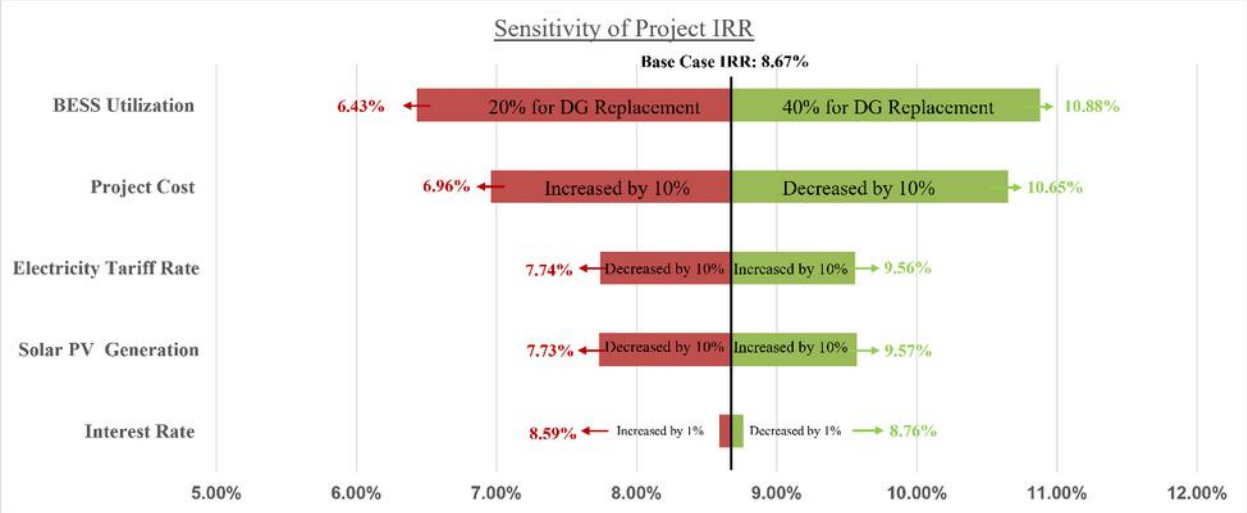


Figure 13: Tornado chart showing sensitivity of the project IRR

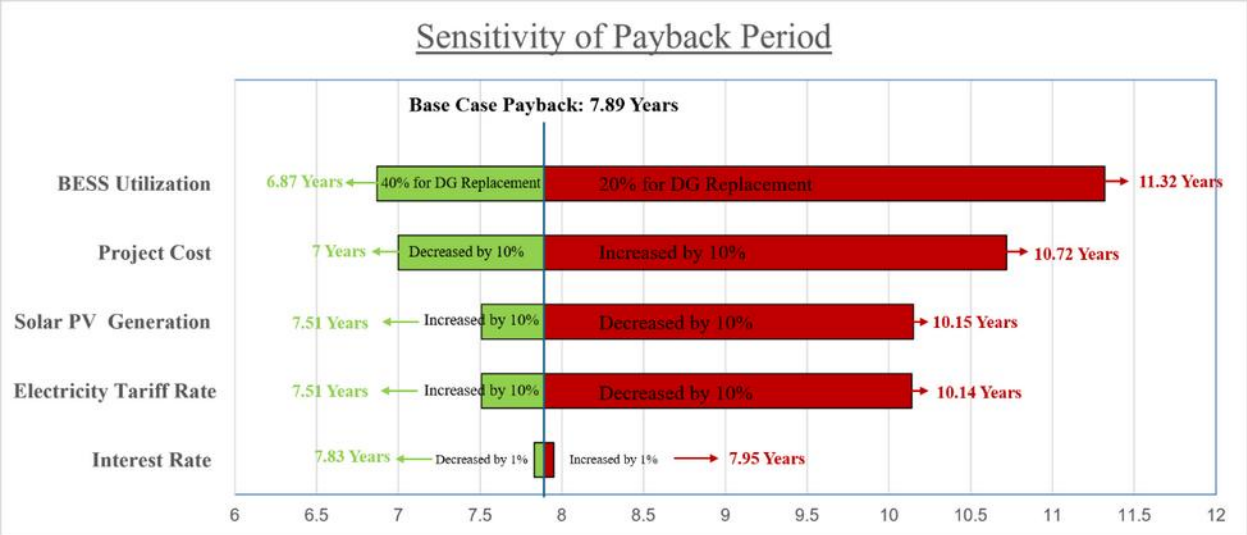


Figure 14: Tornado chart showing sensitivity of the project payback

4.4 Environmental Performance

The proposed PV–BESS system achieved a net annual CO_2-equivalent emission reduction of 308.15 tCO_2-eq/year. As shown in Figure 15, solar PV generation replacing grid electricity contributed the largest reduction of 262.56 tCO_2-eq/year, followed by BESS-based DG displacement, which reduced emissions by 92.09 tCO_2-eq/year. However, BESS operation for peak shaving resulted in an additional 46.52 tCO_2-eq/year of emissions, partially offsetting the overall environmental benefits. These results demonstrate that solar PV integration and reduced reliance on DG are the primary contributors to the system's emission-reduction potential. Figure 15 shows the annual CO_2-eq emission reduction from each sources.

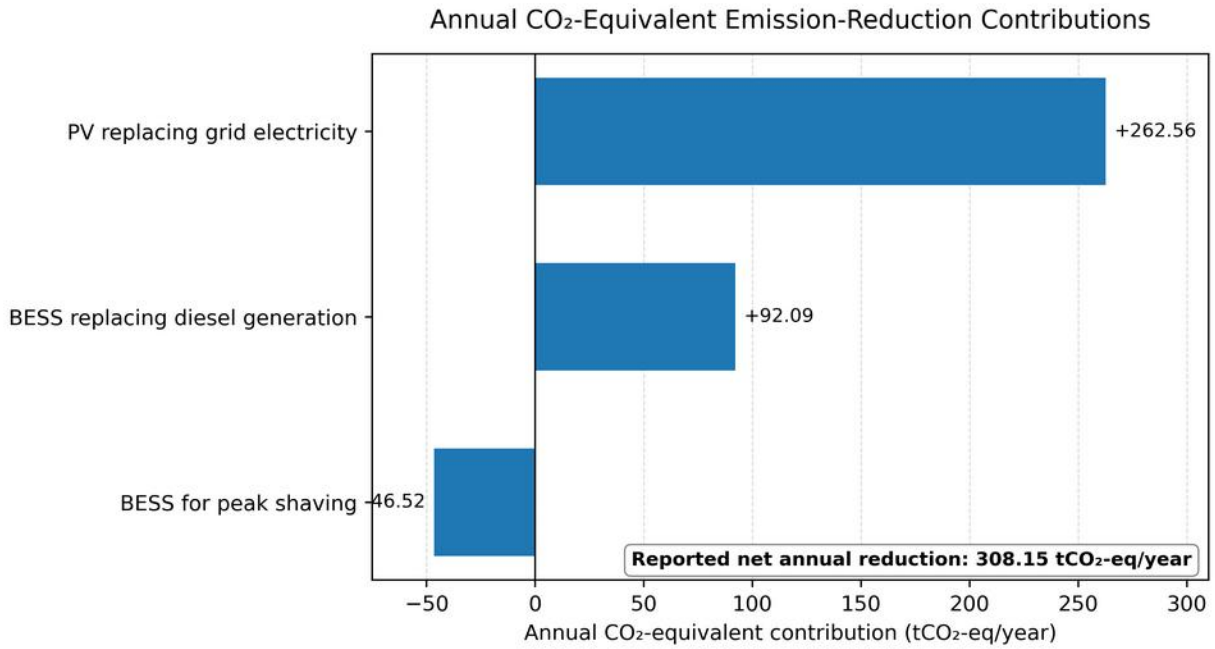


Figure 15: Annual CO2-eq emission reduction contributions

5 Discussions

5.1 PV Performance

The simulated PV output indicates substantial potential for reducing grid electricity purchases. However, the seasonal difference between the highest and lowest monthly generation highlights the importance of evaluating PV performance against the industrial load rather than relying on annual energy production alone. The decline in PR during May, despite peak generation, is consistent with increased temperature-related losses under higher-irradiance conditions. Thus, absolute energy generation and conversion performance should be interpreted separately when assessing seasonal PV performance.

5.2 Significance of the optimized PV-BESS configuration

The optimization results indicate that integrating PV and BESS with the existing grid and DG provides a more economical configuration than the assessed alternatives. The 2450-kWh BESS appears to offer a cost-effective balance between storage capacity, energy shifting and backup capability. The higher-capacity battery configuration did not offset its additional investment through sufficient economic benefits, while the grid–BESS configuration without PV had a higher NPC.

The operating results further demonstrate that the BESS serves two complementary functions: shifting electricity use across periods and supporting the industrial load during grid interruptions. Retaining the existing DG provides an additional backup resource, reducing the need to size the battery exclusively for prolonged outages. These findings underline the importance of optimizing PV capacity, battery size and backup resources together rather than evaluating each component independently.

5.3 Economic Viability and Operational Sensitivity

The initial investment is dominated by the BESS, which accounts for maximum of the combined PV and battery capital cost. Consequently, the economic performance of the proposed system depends substantially on how effectively the battery is utilized. The sensitivity results reinforce this relationship: increasing the BESS allocation for DG replacement improves the reported financial indicators, while reducing that allocation considerably extends the payback period.

Project cost also has a substantial influence on the investment outcome, emphasizing the importance of competitive procurement and appropriate system sizing. By comparison, the relatively small effect of interest-rate variation suggests that, within the assessed range, operational strategy and capital expenditure are more consequential financial drivers. These results also indicate that the assumed balance between DG replacement and peak shaving should be justified against actual outage patterns, generator operation and industrial demand.

The financial findings should therefore be interpreted as scenario-dependent rather than universal. The realized savings will depend on the actual dispatch strategy, electricity tariffs, PV generation, battery utilization and future operating conditions.

5.4 Environmental Implications

The reported emissions reduction suggests that the proposed system can provide environmental benefits alongside potential electricity-cost savings. PV generation contributes through displacement of grid electricity, while battery discharge for DG replacement avoids diesel-generator operation. However, the emissions attributed to peak shaving are negative in the reported assessment, indicating that this operating mode introduces an emissions penalty under the adopted accounting assumptions. This highlights that battery dispatch should be evaluated using both economic and environmental criteria: peak shaving may provide financial benefits without necessarily maximizing emissions reductions. The environmental outcome therefore depends on the source of electricity used to charge the battery and the generation displaced during discharge.

6 Limitations

i) Real-time hourly electricity consumption data were collected for only one month. Although the reconstructed hourly load profile model was validated against available data, the limited duration of real-time data may not fully capture seasonal and operational variations in the industry's electricity demand.

ii) The analysis is based on a single manufacturing industry; therefore, the findings may not be directly generalizable to industries with different electricity demand profiles and operating conditions.

iii) The techno-economic results depend on the input data, electricity tariff structure, and technical and financial assumptions adopted in the simulation. Future changes in electricity tariffs, battery costs and industrial energy demand may influence the projected economic performance.

iv) The long-term economic performance of the system may be affected by variations in battery operating strategies, battery degradation over time and the costs associated with battery replacement during the project lifetime.

7 Conclusion

The study evaluated the techno-economic analysis of a grid-connected solar PV-BESS system for a food products manufacturing industry using the reconstructed load profile generated from actual industrial load data, simulated site-specific solar PV performance and prevailing grid and tariff constraints. Based on the study results, the flowing conclusions are drawn;

i) The industrial facility has significant potential for rooftop solar integration, and the technical assessment confirmed the suitability of a 600 kWp PV system with a 500-kW inverter capacity under the considered rooftop and grid constraints.

ii) The two-stage modelling approach combining PVsyst for site-specific PV system assessment and HOMER Grid for BESS optimization provided an effective framework for evaluating the interaction between solar generation, battery storage, utility grid and DG.

iii) HOMER Grid identified the PV-BESS-grid-DG configuration as the preferred system based on economic performance, demonstrating that battery storage can improve solar utilization while supporting the industrial load during grid interruptions and reducing dependence on DG.

iv) Regmi et al., (2022) reported that a solar PV-BESS-grid-DG configuration was more economically feasible than a solar PV-grid-DG configuration based on the overall system comparison performed in HOMER Grid. In contrast, the present study evaluates the financial performance specifically for the optimized solar PV-BESS configuration. Thus, the financial indicators presented in this study represent the economics of the selected PV-BESS system itself, rather than a comparative HOMER Grid base-case assessment of alternative system configurations. This difference in the assessment approach should be considered when comparing the economic results of the two studies.

v) The optimized PV–BESS system showed an IRR of 8.67% and a payback period of 7.89 years, indicating that the system is leaning towards techno-economic feasibility.

vi) The sensitivity analysis demonstrated that the economic performance of the proposed system is particularly influenced by the allocation and utilization of BESS for DG replacement and peak-shaving applications. This indicates that the economic benefit of battery storage depends strongly on how effectively its available capacity is utilized for different energy-management functions. Therefore, appropriate BESS sizing and operational allocation are important for maintaining the economic feasibility of PV–BESS systems in industrial applications.

8 Acknowledgement

The authors would like to express their sincere gratitude to the Department of Mechanical and Aerospace Engineering, Pulchowk Campus, for its guidance and support throughout this research. The authors also gratefully acknowledge Asian Biscuits and Confectionery Private Limited for providing the necessary data, site access and technical support required for this study.

9 Funding

The author(s) received no financial support for the research, authorship, or publication of this paper.

10 Conflict of Interest

The author(s) declare no conflict of interest.

11 Data Availability

The data supporting the findings of this study are available from the corresponding author upon request.

12 References

Alternative Energy Promotion. (2026). *Leveraging Investment in Sustainable Energy: Achievements of Sustainable Energy Challenge Fund*. Alternative Energy Promotion Centre. https://www.aepc.gov.np/docs/1989/Leveraging%20Investment%20in%20Sustainable%20Energy%20-%20AEPC%20-%20Jan%2022%202026_web.pdf

Boruah, D., & Chandel, S. S. (2024). Techno-economic feasibility analysis of a commercial grid-connected photovoltaic plant with battery energy storage-achieving a net zero energy system. *Journal for Energy Storage*, 77.

Cheng-Yu Peng, Cheng-Chien Kuo, & Chih-Ta Tsai. (2021). Optimal Configuration with Capacity Analysis of PV-Plus-BESS for Behind-the-Meter Application. *Applied Sciences*, 7851.

Chih-Ta Tsai, Erica M. Ocampo, Teketay Mulu Beza, & Cheng-Chien Kuo. (2020). *Techno-Economic and Sizing Analysis of Battery Energy Storage System for Behind-the-Meter Application*. 203734–203746.

Government of Nepal. (n.d.). *District and Local Levels*. Government of Nepal. Retrieved https://giwmscdnone.gov.np/media/pdf_upload/district%20and%20local%20levels_daokv47.pdf

Han, X., Garrison, J., & Hug, G. (2022). Techno-economic analysis of PV-battery systems in Switzerland. *Renewable and Sustainable Energy Reviews*, *158*. https://doi.org/10.1016/j.rser.2021.112028

Hopley, I., Ghahramani, M., & Aziz, A. (2024). Techno-Economic Factors Impacting the Intrinsic Value of Behind-the-Meter Distributed Storage. *Sustainability*, *13*(23). https://doi.org/10.3390/su162310432

International Energy Agency. (2026). *Global Energy Review 2026*. International Energy Agency. https://www.iea.org/reports/global-energy-review-2026

Jivaganont, P., & Mongkoltanatas, J. (2021). PV-ESS design for industrial loads under TOU pricing structure in Thailand. *International Journal of Smart Grid and Clean Energy*, *10*(3). https://doi.org/10.12720/sgce.10.3.167-182

Mansour Alramlawi, Ayeni Femi Timothy, Aouss Gabash, Erfan Mohagheghi, & Pu Li. (2018). Optimal operation of PV-Diesel MicroGrid with multiple diesel generators under grid blackouts. *2018 IEEE International Conference on Environment and Electrical*

Engineering and 2018 IEEE Industrial and Commercial Power Systems Europe (EEEIC/I&CPS Europe), 1–6. https://ieeexplore.ieee.org/document/8494571

Mario Lamagna, Benedetto Nastasi, Daniele Groppi, Meysam Majidi Nezhad, & Davide Astiaso Garcia. (2020). Hourly energy profile determination technique from monthly energy bills. *Building Simulation*, *13*(6), 1235–1248.

Matera, N., Ramaschi, R., Cabrera-Tobar, A., Ogliari, E., & Leva, S. (2025, July 15). A Techno-Economic Assessment of Integrated Photovoltaic Battery Storage Systems for Industrial Applications in Northern Italy. *Conference Proceedings – 2025 IEEE International Conference on Environment and Electrical Engineering and 2025 IEEE Industrial and Commercial Power Systems Europe*. 2025 IEEE International Conference on Environment and Electrical Engineering and 2025 IEEE Industrial and Commercial Power Systems Europe (EEEIC/I&CPS Europe). https://doi.org/10.1109/EEEIC/ICPSEurope64998.2025.11169174

Regmi, B. R., Silwal, B., & Karki, M. (2022). *Optimal techno-commercial analysis on electricity consumption of industry by grid integrated hybrid power system*. 11th IOE Graduate Conference.

Sepúlveda-Mora, Sergio B., Hegedus, & Steven. (2021). Making the case for time-of-use electric rates to boost the value of battery storage in commercial buildings with grid connected PV systems. *Energy*. https://doi.org/10.1016/j.energy.2020.119447

Static and Dynamic Stability Analysis of a Fixed-Wing eVTOL Aircraft

Aniket Kumar Gupt[1*], Adit Gajurel[2], Rohan Magrati[2], Topjang Gharti Magar[2]

[1,2]Department of Mechanical and Aerospace Engineering, Institute of Engineering, Pulchowk Campus, Tribhuvan University
Lalitpur, Nepal
[*]xuav.aniket@gmail.com

Abstract

Safety of operation of electric VTOL air ambulance is strongly dependent upon good aerodynamic stability characteristics and good handling qualities. In this work, static and dynamic stability of new 4,800 kg weight of fixed wing, V-tail eVTOL air ambulance concept with 300 km of mission radius was evaluated. Two-step computational method was used to analyze the aircraft during the flight in fixed-wing configuration: static stability was evaluated by the vortex lattice method in XFLR5, and dynamic stability modes were evaluated via detailed flight simulation in X-Plane 12 at the height of 14,000 ft. Static analysis proved presence of longitudinal, lateral, and directional stability. Analysis of time history of perturbed roll, pitch and yaw movements has shown that dynamic modes Short Period, Phugoid, Dutch Roll, and Spiral have acceptable frequencies and damping ratios. Based on the dynamics of the aircraft under control inputs, eVTOL got Cooper-Harper handling qualities rating of 3. These findings show that while the aircraft has minor but undesirable shortcomings, the need for pilot corrections is low, meeting the requirements for MIL-F-8785C Category B Level 1 stability.

Keywords: eVTOL, static stability, dynamic stability, handling qualities, Cooper-Harper rating

Introduction

The rapid and safe transport of patients during medical emergencies is a critical challenge in extreme geographic environments, disaster zones, and highly congested urban areas. Traditionally, aeromedical evacuation has relied on two distinct platforms: helicopters and conventional fixed-wing aircraft. While helicopters offer essential vertical takeoff and landing (VTOL) capabilities, they are limited by lower cruising speeds and restricted operational ranges. Conversely, conventional fixed-wing aircraft provide speed and efficiency but strictly require established runway infrastructure. To bridge this gap, electric vertical takeoff and landing (eVTOL) architectures have emerged as a transformative solution. By combining distributed electric propulsion with fixed-wing aerodynamics, hybrid eVTOL aircraft present a unique platform capable of rapid, runway-independent deployment and high-speed forward flight (Senwei et al., 2024).

However, the unconventional geometries of heavy-lift eVTOL aircraft such as distributed rotors, high-wing placements, and V-tail empennages introduce highly complex, non-linear flight dynamics. Ensuring the safety of critical medical payloads requires rigorous aerodynamic characterization during the conceptual design phase (Prabhakar, Salucci, & Karbowski, 2021). While extensive research has been conducted on lightweight urban air taxis, there remains a significant research gap regarding the handling qualities and stability of high-capacity (4,800 kg) fixed-wing eVTOLs specifically configured for a 300 km emergency medical services (EMS) mission.

To address this gap, this study presents the conceptual design and stability analysis of a novel 4,800 kg fixed wing eVTOL air ambulance. The primary objective is to evaluate the aircraft's static stability and simulate its dynamic oscillation modes under realistic flight envelopes. Furthermore, this study quantifies pilot workload using the Cooper-Harper rating scale (Cooper & Harper, 1969) to determine if the platform satisfies the handling quality requirements of MIL-F-8785C for Category B flight phases (Department of Defense, 1980).

Literature Review / Related Work

The development of eVTOL aircraft has accelerated rapidly, driven by advancements in battery energy density and distributed electric propulsion. Recent literature emphasizes the transition from simple multirotor designs to Lift-plus-Cruise configurations. Senwei et al. (2024) note that fixed-wing eVTOLs demonstrate superior aerodynamic efficiency and extended range capabilities, which are prerequisites for regional medical transport. Despite these advantages, hybrid configurations experience complex aerodynamic interactions, necessitating robust stability margins (Prabhakar, Salucci, & Karbowski, 2021).

To evaluate these flight dynamics prior to prototyping, aerospace researchers increasingly rely on computational aerodynamic modeling. Vortex lattice methods (VLM), such as those implemented in XFLR5, have become standard for extracting baseline aerodynamic coefficients and determining neutral points. For dynamic responses, system identification utilizing simulation environments like X-Plane has proven highly effective. Johnson et al. (2021) demonstrated the use of non-linear flight dynamics modeling in X-Plane, confirming that simulator-derived time-history data aligns with real-world metrics.

This computational approach has been validated by foundational research at the Institute of Engineering, Tribhuvan University. Karki et al. (2023a) successfully evaluated the dynamic characteristics of fixed-wing UAS platforms, establishing a reliable methodology for extracting natural frequencies and damping ratios.

Translating these metrics into safety standards requires established handling quality criteria. The MIL-F-8785C military specification remains the benchmark for evaluating the flying qualities of piloted airplanes (Department of Defense, 1980). Moorhouse and Woodcock (1982) linked these dynamic responses to pilot workload, which is subjectively quantified using the Cooper-Harper rating scale (Cooper & Harper, 1969).

Position of the Present Study: Existing literature predominantly applies this evaluation framework to lightweight UAVs or conventional aircraft.

Materials and Methods

To conduct an analysis of the flight dynamics of the aircraft ambulance that is being designed, a two-stage process was used, which consisted of computing aerodynamics and flight simulation.

1. Aircraft Architecture and Study Design

The proposed eVTOL platform is a fixed-wing, hybrid Lift-plus-Cruise architecture sized for a Maximum Takeoff Weight (MTOW) of 4,800 kg. It accommodates a seven-person payload (800 kg): one pilot, two stretchered patients, and four medical personnel. The airframe features an 18 m high-wing configuration utilizing a NACA 2412 airfoil (Aspect Ratio 7.2, Area 45 m^2) to maximize lift during transition and cruise. To ensure lateral and directional stability while

minimizing empennage weight, a V-tail geometry utilizing a NACA 0012 airfoil with a 4.8 m span was selected. The aircraft is powered by a 550-kWh distributed electric propulsion system to achieve a 300 km operational range at a cruise speed of 72 m/s.

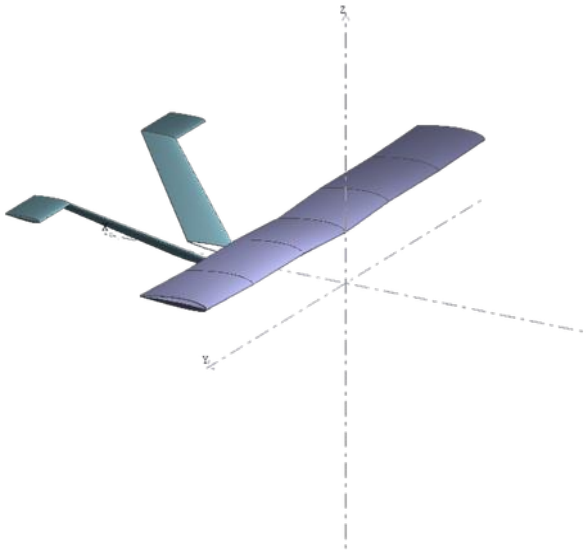


Figure 1: XFLR5 3D



Figure 2: X-Plane 12 3D View

2. Static Stability

Preliminary aerodynamic assessment was conducted using XFLR5 via the Vortex Lattice Method (VLM). A three-dimensional computational model was constructed to extract baseline coefficients. Longitudinal static stability was evaluated by plotting the pitching moment coefficient against the angle of attack. Lateral and directional static stability were verified by determining the rolling moment and yawing moment coefficients relative to the sideslip angle.

3. Dynamic Stability and Handling Qualities Simulation

To capture the non-linear dynamic characteristics, a high-fidelity virtual model was developed and deployed within the X-Plane 12 simulation environment. Flight tests were conducted during steady-state cruise at an operational altitude of 14,000 ft. Dynamic perturbations were manually introduced via step and doublet inputs to the control stick, exciting the Short Period, Phugoid, Dutch Roll, and Spiral modes. The simulator recorded the time-history data of the pitch, roll, and yaw rates. The resulting damping ratios and natural frequencies were evaluated against MIL-F-8785C Category B flight phases. Finally, pilot workload was quantified using the Cooper-Harper rating scale based on the system's response to the induced disturbances.

Results

1. Static Stability

The vortex lattice analysis confirmed that the proposed eVTOL geometry possesses the necessary inherent restoring tendencies for safe flight. The longitudinal analysis demonstrated a negative pitching moment slope (), ensuring pitch stability. The V-tail and dihedral configuration successfully generated a negative rolling moment slope () for lateral stability and a positive yawing moment slope () for directional (weathercock) stability. The analytically determined neutral point provided a safe static margin, confirming that the aircraft remains stable across its full CG travel limits.

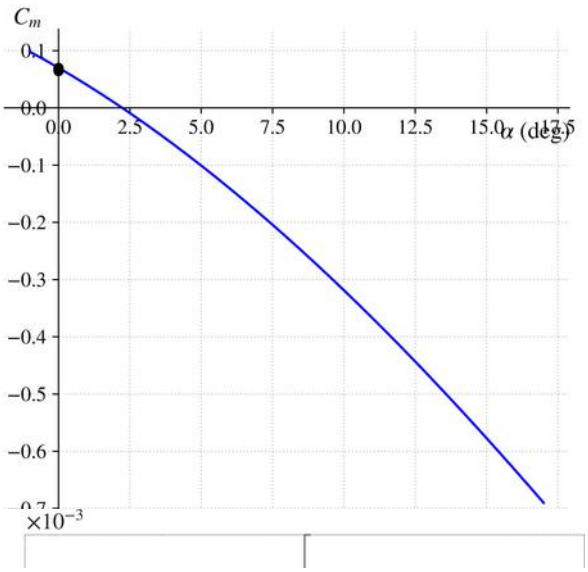


Figure 3: Static Longitudinal Stability

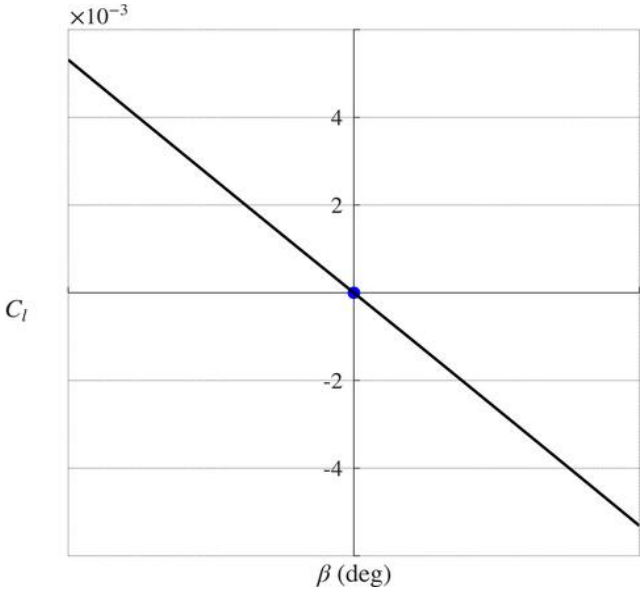


Figure 4: Static Lateral Stability

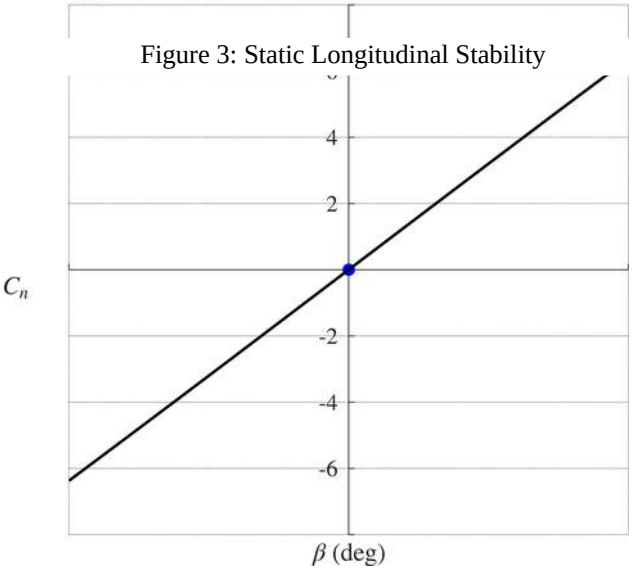


Figure 5: Static Directional Stability

2. Dynamic Stability

The time-history data extracted from the X-Plane 12 simulations demonstrated favorable damping characteristics across all primary dynamic modes. The natural frequencies and damping ratios for the 14,000 ft test altitude are detailed in Table 1.

Table 1

Dynamic Stability Characteristics at High Altitude (14,000 ft)

Dynamic Mode	Frequency (Hz)	Damping Ratio	Subsidence Ratio
Short Period	0.3485	0.3421	0.7971
Phugoid	0.0216	0.0534	0.0069
Dutch Roll	0.3125	0.1556	0.3092

Note. Data derived from simulated stick perturbation responses in X-Plane 12.

The Spiral mode analysis indicated a slow, manageable rate of roll divergence or convergence that fell well within allowable pilot reaction times, mitigating the risk of a rapid, uncontrollable spiral dive.

3. Handling Qualities

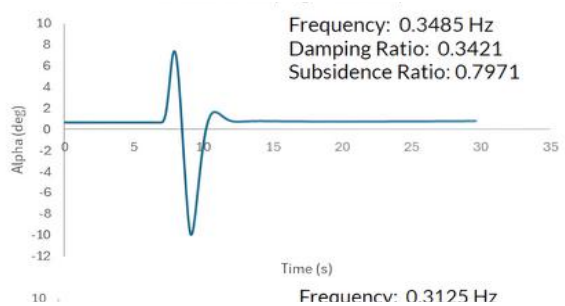


Figure 6: Short Period Mode

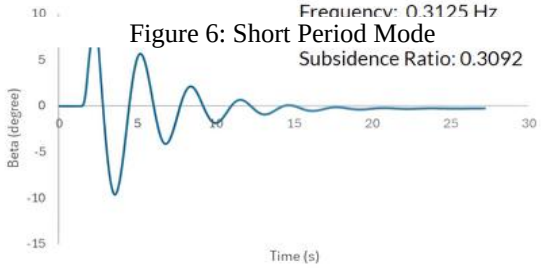


Figure 8: Dutch Roll Mode

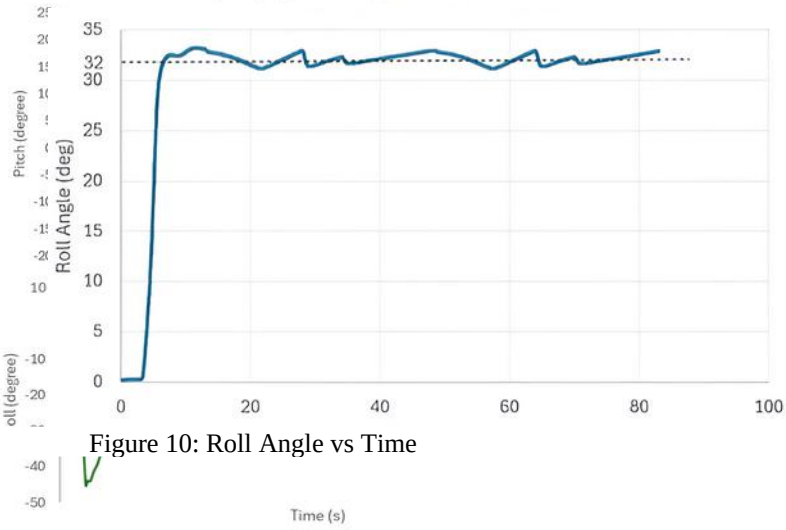


Figure 10: Roll Angle vs Time

Figure 9: Spiral Mode

Based on the aircraft's response to dynamic mode excitation and the required pilot compensation to maintain a stable flight path, the eVTOL achieved a rating of 3 on the Cooper-Harper Rating Scale. This categorizes the platform as having Level 1 stability under the MIL-F-8785C criteria for Category B flight phases.

Discussion

The results of the static and dynamic analyses validate the aerodynamic viability of the 4,800 kg eVTOL concept for aeromedical missions. The static margin confirmed by XFLR5 ensures that the aircraft is inherently stable without being excessively nose-heavy, which could otherwise lead to sluggish control responses and pilot fatigue.

The dynamic simulation results closely align with the stringent requirements for utility transport aircraft. The Short Period mode is heavily damped at the tested 14,000 ft altitude envelope (damping ratio > 0.32), which is critical for preventing pilot-induced oscillations (PIO) during sudden pitch maneuvers or turbulent atmospheric conditions. While the Phugoid mode is lightly damped (ratio ~0.05), its highly gradual, low-frequency oscillation (0.02 Hz) allows the pilot or flight control computer to easily correct altitude deviations without conscious effort.

Furthermore, the V-tail configuration proved highly effective at suppressing adverse yaw-roll coupling, as evidenced by the rapid damping of the Dutch Roll mode. Consequently, the Cooper-Harper rating of 3 accurately reflects that while the aircraft exhibits the mild, unpleasant deficiencies standard to large, high-wing hybrid architectures, it requires minimal pilot compensation to achieve the desired performance. Meeting the Level 1 stability criteria for MIL-F-8785C Category B flights ensures that the pilot can safely navigate the aircraft during the cruise, climb, and descent phases required for emergency patient transport.

Limitations

While computational fluid dynamics and flight simulation provide robust conceptual validation, these methods present inherent limitations. The Vortex Lattice Method (VLM) utilized by XFLR5 assumes inviscid, attached flow, meaning the static stability margins may lose fidelity at high angles of attack or in post-stall regimes. Additionally, within the X-Plane 12 environment, dynamic modes were excited via manual stick inputs rather than precise mathematical impulses. This introduces minor variances in the initial perturbation amplitudes, though the resulting natural frequencies and damping ratios remain statistically valid for conceptual characterization.

Conclusion

This study successfully established the aerodynamic viability of a 4,800 kg fixed-wing eVTOL air ambulance. The XFLR5 analysis confirmed that the high-wing and V-tail architecture provides robust static longitudinal, lateral, and directional stability margins. Subsequent flight simulations in X-Plane 12 verified that the aircraft's Short Period, Phugoid, Dutch Roll, and Spiral modes exhibit favorable damping characteristics at its standard cruising altitude of 14,000 ft. By achieving a Cooper-Harper rating of 3, the platform requires minimal pilot workload, fulfilling the stringent Level 1 stability requirements of MIL-F-8785C for Category B flight phases. These findings validate the conceptual design as a safe, highly reliable platform for critical aeromedical evacuation missions, laying the foundation for future sub-scale prototyping and automated flight control system integration.

Acknowledgments

The authors gratefully acknowledge the Department of Mechanical and Aerospace Engineering at the Institute of Engineering, Pulchowk Campus, Tribhuvan University, for providing the software tools and technical resources required to conduct this research.

Funding

The author(s) received no financial support for the research, authorship, or publication of this paper.

Conflict of Interest

The author(s) declare no conflict of interest.

Data Availability

The XFLR5 aerodynamic coefficient datasets and X-Plane 12 flight simulation logs generated during this study are available from the corresponding author upon reasonable request.

References

Cooper, G. E., & Harper, R. P. (1969). *The use of pilot rating in the evaluation of aircraft handling qualities* (NASA TN D-5153). National Aeronautics and Space Administration. https://apps.dtic.mil/sti/citations/AD0689722

Department of Defense. (1980). *Military specification: Flying qualities of piloted airplanes* (MIL-F-8785C). United States Department of Defense.

Johnson, E. N., et al. (2021). System identification of a nonlinear flight dynamics model for a small fixed-wing UAV. *Aerospace Science and Technology*, *115*, 106795.

Karki, A., Bhattrai, S., & Darlami, K. (2023a). Dynamic characteristics and flying quality assessment of twin-boom fixed-wing unmanned aerial system. *Department of Mechanical and Aerospace Engineering, Tribhuvan University*.

Karki, A., Darlami, K., & Bhattrai, S. (2023b). Conceptual design and stability analysis of a fixed wing UAS research platform for aerial experiments. *Department of Mechanical and Aerospace Engineering, Tribhuvan University*.

Laminar Research. (2022). *X-Plane 12 desktop manual*. https://x-plane.com/manuals/desktop/

Moorhouse, D. J., & Woodcock, R. J. (1982). *Background information and user guide for MIL-F-8785C, military specification-flying qualities of piloted airplanes*. Air Force Wright Aeronautical Labs. https://apps.dtic.mil/sti/citations/ADA119421

Prabhakar, N., Salucci, F., & Karbowski, D. (2021). Simulating system and powerplant dynamics of an e-VTOL aircraft including transition. In *AIAA Aviation 2021 Forum* (p. 3183). American Institute of Aeronautics and Astronautics. https://doi.org/10.2514/6.2021-3183

Senwei, S. Y., et al. (2024). The ongoing evolution of EVTOLs: Urban transport potential and emergency response. *Urban Air Mobility Journal*, *2*(1), 45-60.

Free Vibration Analysis of an Inverted L-Shaped Frame Structure

Surya Prasad Kafle[1*], Mahesh Chandra Luintel[1], Rajesh Kaji Kayasta[1]

[1]Department of Mechanical and Aerospace Engineering, Pulchowk Campus, Institute of Engineering, Tribhuvan University
Lalitpur, Nepal
080msmde024.surya@pcampus.edu.np,mcluintel@ioe.edu.np,rajeshkajikayastha@gmail.com

Abstract

Inverted L-shaped frames are widely used as machine supports, sign and signal posts and structural brackets, where resonance can cause fatigue failure. This study investigates the free vibration characteristics of a mild steel inverted L-shaped frame of square hollow section (50.8 mm × 2 mm), with a 1000 mm vertical member and an 800 mm horizontal member, in two configurations: without support and with a knee brace placed 300 mm from the welded corner. Finite element modal analysis was carried out in ANSYS 2019 R3 with a fixed base, and the first three natural frequencies and mode shapes were extracted. Specimens of both configurations were fabricated and tested by impact hammer excitation, with the response measured by an accelerometer, charge amplifier and NI data acquisition system in LabVIEW and transformed to the frequency domain in MATLAB. For the unbraced frame, the measured frequencies (12.37, 94.90 and 211.59 Hz) agreed with the numerical values (13.85, 94.11 and 205.71 Hz) within 0.84% and 2.78% for the second and third modes, while the first mode differed by 11.96%, attributed mainly to base fixity and joint idealisation. Numerically, the knee brace raised the first three natural frequencies by 11.42%, 26.90% and 24.49% because it stiffens the corner while adding little mass. The measured frequencies of the braced specimen, however, were nearly identical to those of the unbraced specimen, so the numerical predictions for the braced frame could not yet be confirmed experimentally; possible causes and the measures needed to verify them are discussed.

Keywords: Free vibration, Inverted L-shaped frame, Knee brace, Modal analysis, Finite element method

Introduction

Frame structures are widely used in mechanical, civil and aerospace engineering because they carry loads efficiently and are simple to fabricate. Among the various configurations, L-shaped and inverted L-shaped frames are common in industrial piping systems, machine frames, structural supports, traffic signal posts, signboards and equipment mounts. Such frames are routinely exposed to dynamic loads from rotating machinery, wind, traffic and seismic activity. If an excitation frequency approaches a natural frequency of the frame, resonance can produce large amplitudes, noise, fatigue cracking and eventual failure. Knowledge of the natural frequencies and mode shapes is therefore essential for safe design.

Vibration characteristics are usually obtained either by numerical simulation, most often the finite element method (FEM), or by experimental modal testing. Numerical models can be built and modified quickly, but they rely on idealised boundary conditions, joint stiffness and material properties, so their predictions must be validated against measurements before they can be trusted for design. Experimental testing captures the real behaviour of the structure, including

manufacturing imperfections and imperfect supports, but it is more time-consuming and is itself affected by measurement errors.

A simple and common way to stiffen an L-shaped frame is to add a diagonal knee brace near the corner. Knee bracing has been studied extensively for the seismic resistance of building frames, but comparatively few studies have examined its effect on the free vibration of an isolated inverted L-shaped frame, and fewer still have compared numerical predictions with laboratory measurements on fabricated specimens. The objective of this study is therefore to investigate and compare the free vibration characteristics of an inverted L-shaped frame with and without knee-braced support using both finite element simulation and experiment. The specific objectives are to fabricate both frame configurations with a fixed base, to determine their first three natural frequencies and mode shapes in ANSYS and by impact testing, and to compare and validate the numerical results against the experimental data.

Literature Review

Several studies have addressed the dynamics of L-shaped beams and frames. Sasaki et al. (2015) used an inverted L-shaped post-buckled beam as a nonlinear passive vibration isolator and, through static tests, free vibration tests, harmonic base excitation and finite element modelling, achieved a fundamental resonance about 80% lower than that of a comparable linear isolator. Bachoo (2021) developed a wave-based analytical model for the in-plane free vibration of non-symmetrically laminated cross-ply L-shaped frames, validated it with ANSYS APDL, and showed that natural frequencies increase with the number of laminate layers. Khanal and Chaulagain (2020) showed numerically that L-shaped reinforced concrete buildings experience larger displacement, drift and torsion than regular buildings under different angles of seismic incidence, although their study had no experimental validation.

Frequency-based studies of beams and frames also show how sensitive natural frequencies are to local changes in stiffness. Zhu and He (2013) detected joint, member and boundary damage in an aluminium space frame with L-shaped beams and bolted joints from changes in natural frequencies, finding that loosened bolts shift the frequencies by up to 8.36%. Kateel (2018) predicted the natural frequencies and frequency response functions of cracked L-shaped beams with a MATLAB finite element model, validated against ANSYS within about 2.31%. Related work on cracked beams (Khaji, 2015; Khnaijar & Benamar, 2017; Pawar, 2013; Toan, 2014) consistently reports that a reduction of local stiffness lowers the natural frequencies, with the effect depending on the location of the change relative to the fixed end and the mode shape.

Knee bracing has mainly been investigated for seismic resistance. Balendra et al. (1990) introduced the knee-brace frame, in which a diagonal brace provides lateral stiffness while a ductile knee element dissipates energy, and confirmed its performance by pseudodynamic testing. Subsequent large-scale tests (Balendra et al., 1997; Sam et al., 1995) showed that properly designed knee-braced frames dissipate substantial energy without significant loss of strength or stiffness. Mofid and Lotfollahi (2006) and Leelataviwat et al. (2011) proposed design procedures for knee geometry, while Sheidaii (2016) showed that knee length and knee moment of inertia strongly influence ductility and collapse probability. Comparative studies of bracing systems (Nongsiej, 2022; Sahu, 2018), energy-absorbing elements (Jurukovski, 1995) and buckling-restrained knee braces (Shin, 2012) confirm that bracing substantially increases lateral stiffness and reduces displacement.

The literature therefore establishes that knee bracing increases structural stiffness and that L-shaped members are sensitive to changes in joint and boundary stiffness. However, most studies are either purely numerical or concern multi-storey building frames under seismic loading. Experimental validation of the free vibration behaviour of a simple inverted L-shaped frame, with and without a knee brace, remains limited, and this gap is addressed in the present study.

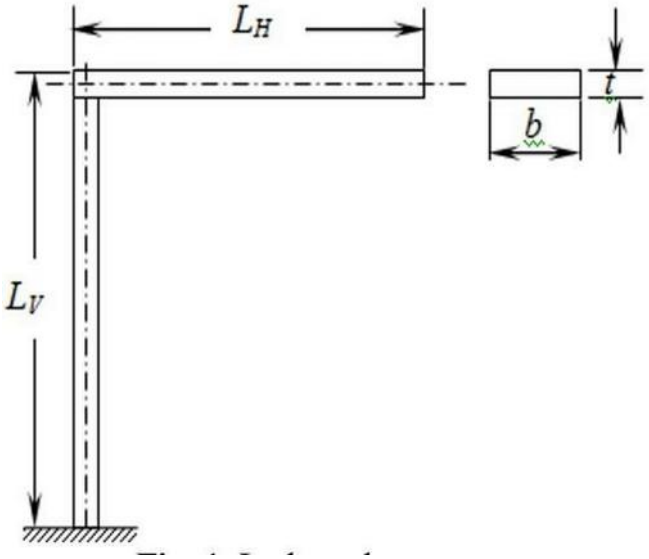
Materials and Methods

Specimen Design and Fabrication

The structural configuration, fixed-free boundary condition and arm length ratio of about 0.8 were adopted from Kateel (2018), while the material, cross-section and method of analysis were chosen for ease of laboratory-scale fabrication. The frame consists of a 1000 mm vertical member and an 800 mm horizontal member made of mild steel square hollow section (SHS) with an outer dimension of 50.8 mm and a wall thickness of 2 mm, joined by arc welding at the corner (Figure 1). The vertical member was welded to a rigid base plate to provide a fixed support. A second, identical frame was fabricated with a knee brace of the same section welded between points 300 mm from the corner on both members, giving a brace length of 424.26 mm at 45°. The fabricated specimens are shown in Figure 2 and their properties are listed in Table 1.

Figure 1

Geometry of the Inverted L-Shaped Frame



Note. L_v = vertical length, L_h = horizontal length, b = outer width and t = wall thickness of the section.

Figure 2

Fabricated Specimens



Table 1

Specimen Specification and Material Properties

Parameter	Value
Material	Mild steel, square hollow section (SHS)
Young's modulus, E	200 GPa
Density, ρ	7850 kg/m^3
Poisson's ratio, ν	0.27–0.30
Outer dimension, b	50.8 mm
Wall thickness, t	2 mm
Vertical length, L_v	1000 mm
Horizontal length, L_h	800 mm
Knee brace length	424.26 mm
Brace position from welded corner	300 mm along both members

Theoretical Background

For an undamped linear structure discretised into finite elements, free vibration is governed by the eigenvalue problem

(1)

where [K] and [M] are the global stiffness and mass matrices, ω_n is the n-th natural circular frequency and $\{\varphi\}_n$ is the corresponding mode shape. For a single mode, the natural frequency in hertz can be expressed in terms of the modal stiffness k and modal mass m as

(2)

Equation (2) shows that adding a member which increases stiffness more than it increases the effective mass raises the natural frequency. The agreement between the experimental frequency f_{exp} and the numerical frequency f_{FEM} was quantified by the percentage difference

(3)

Numerical Modelling

The two frames were modelled in SOLIDWORKS and imported into ANSYS 2019 R3 (Figure 3). A linear elastic material model with the properties of Table 1 was assigned, and no additional mass was included. The base of the vertical member was assigned a fixed support, and the horizontal member was left free. The geometry was discretised with triangular elements, refined at the corner and edges where the stress gradients are highest, giving 144,480 nodes and 69,029 elements. Modal analysis was performed with the Mechanical APDL solver, and the first three natural frequencies and mode shapes were extracted for each configuration.

Figure 3

Finite Element Models of the Frame



(a) Without knee brace

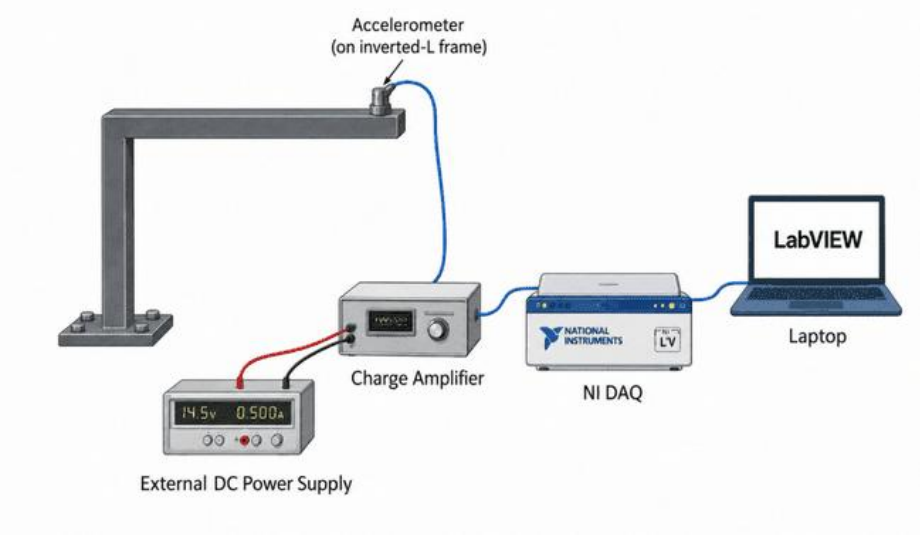
(b) With knee brace

Experimental Setup and Procedure

The experimental setup (Figure 4) consisted of the frame specimen, a piezoelectric accelerometer, a charge amplifier powered by a 4.5 V DC supply, an NI data acquisition (DAQ) system, an impact hammer and a laptop running LabVIEW. The base plate was rigidly clamped to satisfy the fixed boundary condition, and the accelerometer was mounted near the free end of the horizontal member, where the response is largest. The frame was excited with the impact hammer, and the time-domain acceleration was recorded in LabVIEW. The signals were converted to the frequency domain by fast Fourier transform (FFT) in MATLAB, and the first three natural frequencies were identified from the spectral peaks. The same procedure was applied to both configurations. The instruments used are shown in Appendix A.

Figure 4

Experimental Setup for Free Vibration Testing



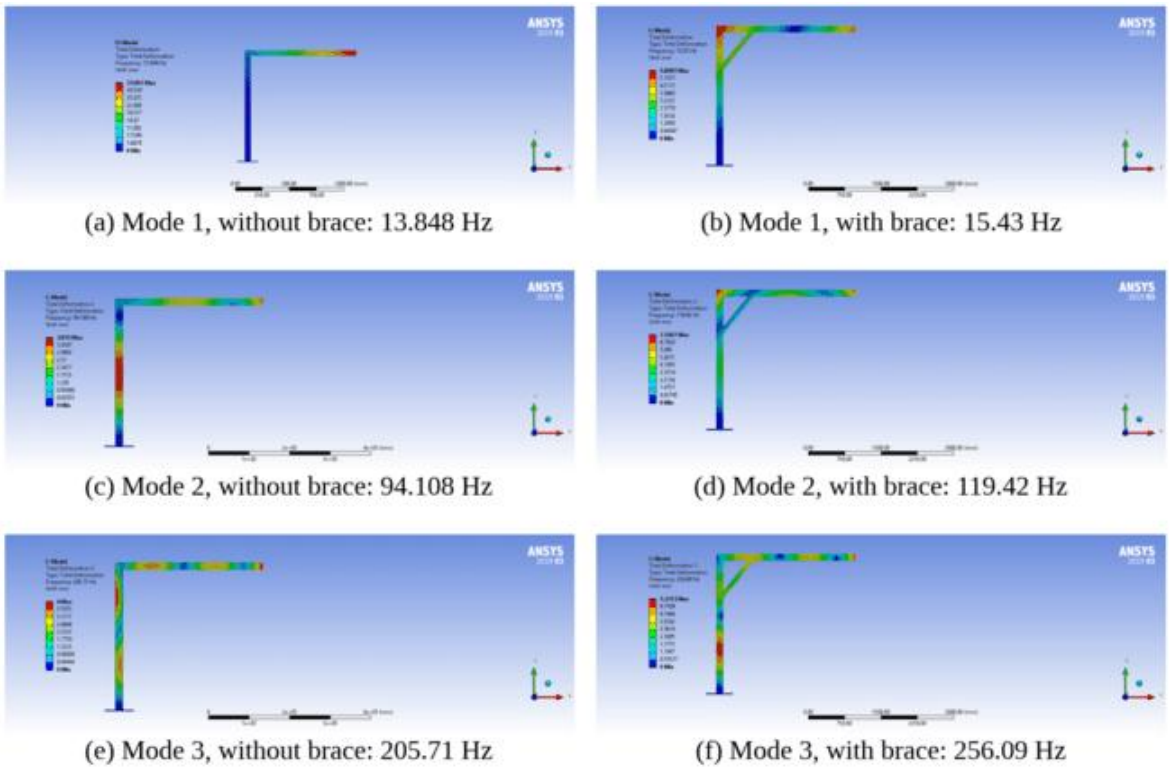
Results

Numerical Natural Frequencies and Mode Shapes

The first three mode shapes obtained from ANSYS for both configurations are shown in Figure 5, and the corresponding natural frequencies are listed in Table 2. For the unbraced frame, the first mode (13.848 Hz) shows deformation concentrated along the horizontal member, while the second (94.108 Hz) and third (205.71 Hz) modes involve higher-order bending of both members. With the knee brace, the frequencies rose to 15.43, 119.42 and 256.09 Hz, increases of 11.42%, 26.90% and 24.49%, and the maximum deformation moved towards the free end of the horizontal member and away from the braced corner.

Figure 5

First Three Mode Shapes Obtained from ANSYS



(a) Mode 1, without brace: 13.848 Hz

(b) Mode 1, with brace: 15.43 Hz

(c) Mode 2, without brace: 94.108 Hz

(d) Mode 2, with brace: 119.42 Hz

(e) Mode 3, without brace: 205.71 Hz

(f) Mode 3, with brace: 256.09 Hz

Table 2

Natural Frequencies Obtained from ANSYS

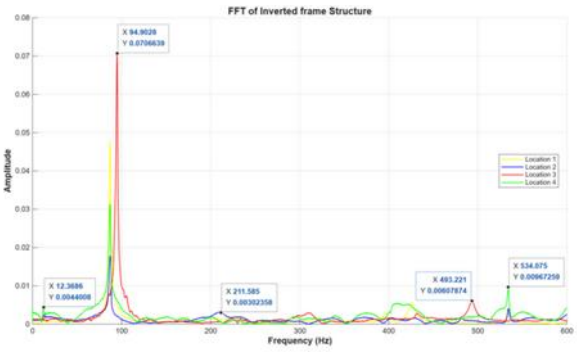
Mode	Without brace (Hz)	With knee brace (Hz)	Difference (Hz)	Increase (%)
1	13.848	15.43	1.582	11.42
2	94.108	119.42	25.312	26.90
3	205.71	256.09	50.380	24.49

Experimental Natural Frequencies

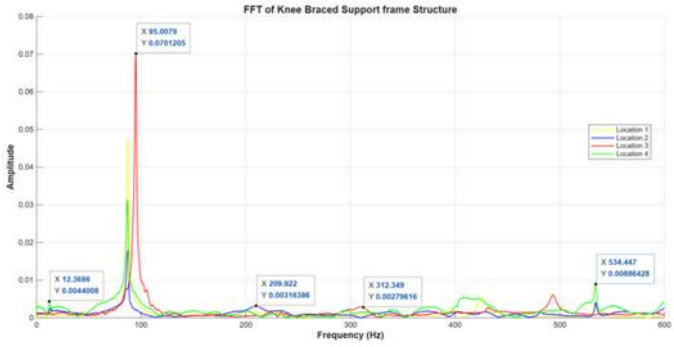
The frequency spectra measured for both configurations are shown in Figure 6. For the unbraced frame, the first three peaks occurred at 12.3686, 94.9028 and 211.585 Hz. For the knee-braced frame, the peaks occurred at 12.3686, 95.0079 and 209.992 Hz. The second-mode peak dominates both spectra, which is consistent with the accelerometer being located near the free end of the horizontal member.

Figure 6

Measured Frequency Spectra (FFT) of the Frame



(a) Without knee brace



(b) With knee brace

Comparison of Numerical and Experimental Results

Table 3 and Figure 7 compare the experimental and numerical frequencies. For the unbraced frame, the second and third modes agree within 0.84% and 2.78%, while ANSYS overestimates the first mode by 11.96%. For the knee-braced frame, the differences are much larger (21.95% to 25.69%) because the measured frequencies did not increase as predicted. Figure 8 shows the effect of the knee brace on both sets of results: ANSYS predicts an increase of 11–27% in every mode, whereas the measured frequencies of the two specimens differ by less than 1%.

Table 3

Comparison of Experimental and Numerical Natural Frequencies

Configuration	Mode	Experimental (Hz)	ANSYS (Hz)	Difference (%)
Without brace	1	12.3686	13.848	11.96
	2	94.9028	94.108	0.84
	3	211.585	205.71	2.78
With knee brace	1	12.3686	15.43	24.75
	2	95.0079	119.42	25.69
	3	209.992	256.09	21.95

Note. Difference calculated with Equation (3), relative to the experimental value.

Figure 7

Experimental and Numerical Natural Frequencies

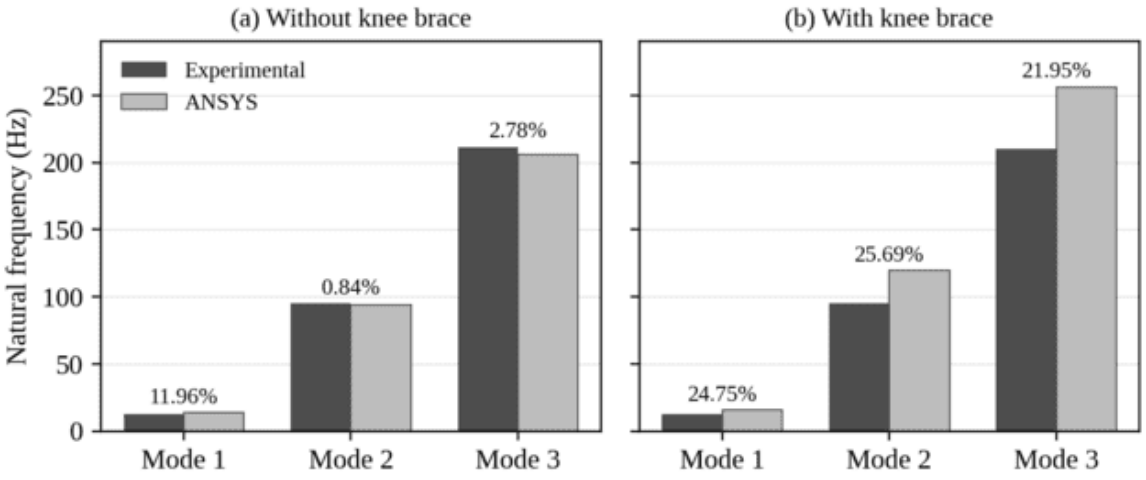
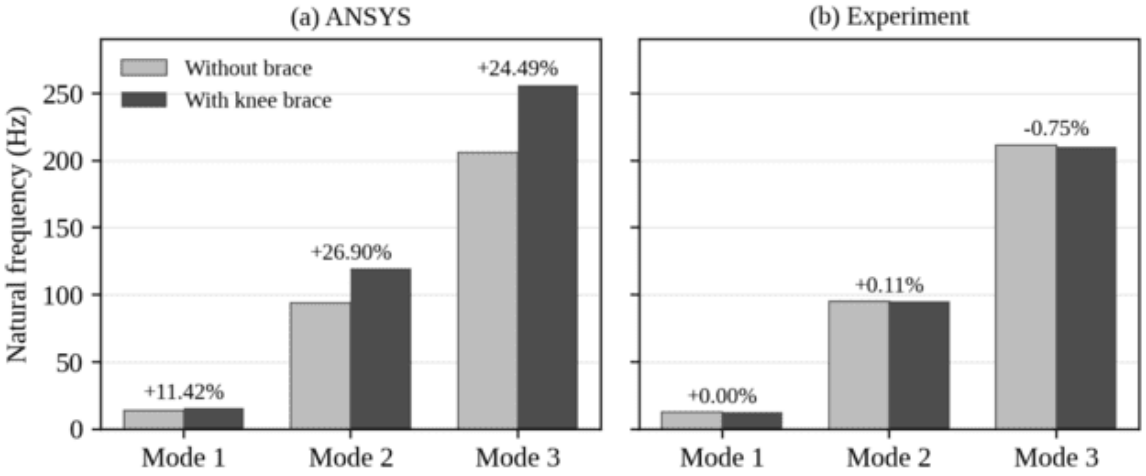


Figure 8

Effect of the Knee Brace on the Natural Frequencies



Discussion

The numerical results show clearly why a knee brace stiffens an inverted L-shaped frame. Without a brace, a load at the free end produces a bending moment that is carried around the corner into the vertical member, so much of the tip deflection comes from rotation of the column top rather than from bending of the horizontal member itself. The knee brace forms a triangle with the two members near the corner. Because a triangle can only deform if one of its sides changes length, part of the corner moment is carried as axial force in the brace, and the axial stiffness of a member is far greater than its bending stiffness. The brace also shortens the effective flexible lengths of both members. The brace adds only about 1.3 kg of mass, and that mass is located near the corner where modal displacements are small, so by Equation (2) the stiffness gain raises the natural frequencies. This agrees with the seismic studies of knee-braced frames, in which the brace is the main source of lateral stiffness (Balendra et al., 1990; Balendra et al., 1997).

The smaller increase in the first mode (11.42%) than in the second and third modes (26.90% and 24.49%) is consistent with this mechanism. The brace lies in the plane of the frame and is most effective against in-plane bending at the corner. If the first mode involves out-of-plane bending of the horizontal member combined with twisting of the column, which is plausible because the torsional stiffness of the section is lower than its bending stiffness, the in-plane brace would contribute relatively little to it. Examining the directional deformation and participation factors of each mode in ANSYS would confirm the mode types.

For the unbraced frame, the close agreement in the second and third modes indicates that the finite element model represents the stiffness and mass distribution of the structure well. The larger first-mode difference, with ANSYS higher than the measurement, indicates that the real frame is more flexible than the model. The most likely cause is the boundary condition: the model assumes a perfectly rigid base, whereas a clamped or welded base plate always permits some rotation, and the first mode carries the largest base moment and is therefore most sensitive to it. Other contributing factors are the stiffness of linear triangular elements in a thin 2 mm wall, the difference between nominal and actual wall thickness and corner radii of the section, the local flexibility and distortion of the welded corner, and the mass of the accelerometer and cable. Damping has a negligible effect on the natural frequencies of a lightly damped steel frame and does not explain the differences.

The experimental results of the knee-braced frame need careful interpretation. The measured frequencies were almost identical to those of the unbraced frame, and the first-mode peak occurred at exactly the same frequency (12.3686 Hz) in both tests, whereas the numerical model predicts an increase of 11–27%. Possible explanations include flexibility of the base clamp dominating the low-frequency response of both specimens, incomplete load transfer through the brace welds, the coarse frequency resolution of the FFT, or a mix-up in the recorded data sets. Until these are checked, by repeating the braced test, measuring the static tip stiffness of both frames and comparing mode shapes with the modal assurance criterion, the numerical prediction of the stiffening effect of the knee brace should be regarded as not yet experimentally validated.

Limitations

The base was idealised as a fixed support in the numerical model, whereas the physical base can rotate slightly and may affect the measured frequencies. The study considered free vibration only, without damping or forced excitation. The welded corner and brace joints were modelled as perfectly bonded, although welding can introduce distortion, residual stress and local stiffness changes. Only one brace configuration (a single brace at 300 mm) and one material and section were examined, and linear elastic material behaviour was assumed. The material properties and mesh size were nominal and were not calibrated, and natural frequencies were compared without mode shape correlation. These factors may account for part of the differences between the numerical and experimental results.

Conclusion

The free vibration characteristics of an inverted L-shaped mild steel frame with and without a knee brace were investigated by finite element simulation and impact testing. For the unbraced frame, the finite element model agreed with the experiment within 0.84% and 2.78% for the second and third modes, and within 11.96% for the first mode, the larger first-mode difference being attributable mainly to base fixity and joint idealisation. The numerical model therefore

represents the unbraced frame reasonably well. The finite element analysis shows that a knee brace placed 300 mm from the corner increases the first three natural frequencies by 11.42%, 26.90% and 24.49% by stiffening the corner region with little added mass, which can be used to move the natural frequencies away from a critical excitation range. The measured frequencies of the braced specimen, however, did not show this increase, so further testing is required before the stiffening effect can be considered experimentally validated.

Future work should repeat the braced-frame tests with verified base fixity and data records, update the finite element model with measured base and joint stiffness, use shell or higher-order elements with a mesh convergence study, compare mode shapes using the modal assurance criterion, and examine the effect of brace position, size and orientation, as well as damping and forced response.

Acknowledgments

We would like to thank Prof. Dr. Surya Prasad Adhikari, Mr. Sudip Bhattarai, Head of the Department, and Mr. Kamal Darlami for their guidance and support. We would also like to thank the Department of Mechanical and Aerospace Engineering, Pulchowk Campus, Institute of Engineering, for providing the workshop and laboratory facilities for fabrication and testing.

Funding

We received no financial support for the research, authorship, or publication of this paper.

Conflict of Interest

We declare no conflict of interest.

Author Contributions

Surya Prasad Kafle: conceptualization, methodology, fabrication, experimental investigation, numerical simulation, formal analysis and writing of the original draft.

Mahesh Chandra Luintel and Rajesh Kaji Kayasta: supervision, methodology, validation, and review and editing of the manuscript.

Data Availability

The experimental data and numerical models supporting the findings of this study are available from the corresponding author on reasonable request.

References

Bachoo, R. (2021). Free vibration analysis of nonsymmetrically laminated cross-ply L-shaped frames. *Proceedings of the Institution of Mechanical Engineers, Part L: Journal of Materials: Design and Applications*. https://doi.org/10.1177/14644207211016888

Balendra, T., Lim, E. L., & Liaw, C. Y. (1997). Large-scale seismic testing of knee-brace-frame. *Journal of Structural Engineering, 123*(1), 11–19. https://doi.org/10.1061/(ASCE)0733-9445(1997)123:1(11)

Balendra, T., Sam, M. T., & Liaw, C. Y. (1990). Diagonal brace with ductile knee anchor for aseismic steel frame. *Earthquake Engineering & Structural Dynamics, 19*(6), 847–858.

Jurukovski, D. (1995). Energy absorbing elements in regular and composite steel frame structures. *Engineering Structures, 17*(5), 319–333.

Kateel, M. C. S. (2018). Mathematical modelling for dynamic analysis of cracked L-shaped beam. *Vibroengineering Procedia, 19*.

Khaji, S. (2015). An analytical method for crack detection of Timoshenko beams with multiple open cracks using a test mass. *European Journal of Environmental and Civil Engineering, 21*(1), 24–41.

Khanal, B., & Chaulagain, H. (2020). Seismic elastic performance of L-shaped building frames through plan irregularities. *Structures, 27*, 22–36.

Khnaijar, A., & Benamar, R. (2017). A new model for beam crack detection and localization using a discrete model. *Engineering Structures, 150*, 221–230.

Leelataviwat, S., Suksan, B., Srechai, J., & Warnitchai, P. (2011). Seismic design and behavior of ductile knee-braced moment frames. *Journal of Structural Engineering, 137*(5), 579–588.

Mofid, M., & Lotfollahi, M. (2006). On the characteristics of new ductile knee bracing systems. *Journal of Constructional Steel Research, 62*(3), 271–281.

Nongsiej, E. T. (2022). Analysis of knee-braced, X-braced moment frame for ductility based seismic design. In *Earthquakes and structures* (Lecture Notes in Civil Engineering, pp. 113–129). Springer.

Pawar, S. S. (2013). Vibrational analysis of cracked cantilever beam subjected to harmonic force by finite element method. *International Journal of Engineering Research and Technology, 5*(2), 2756–2760.

Sahu, K. S. (2018). Nonlinear dynamic analysis of steel building using different types of bracing system. *International Research Journal of Engineering and Technology, 5*(12), 833–838.

Sam, M. T., Balendra, T., & Liaw, C. Y. (1995). Earthquake-resistant steel frames with energy dissipating knee elements. *Engineering Structures, 17*(5), 334–343.

Sasaki, T., Waters, T., & Tsuji, Y. (2015). Experimental study on a nonlinear vibration isolator based on a post-buckled inverted L-shaped beam. *Mechanical Engineering Journal, 2*(3), Article 15-00030. https://doi.org/10.1299/mej.15-00030

Sheidaii, M. (2016). Investigation of the non-linear seismic behavior of knee braced frames using the incremental dynamic analysis method. *International Journal of Advanced Structural Engineering, 8*, 151–159.

Shin, J. (2012). Experimental study on buckling-restrained knee brace with steel channel sections. In *Proceedings of the 15th World Conference on Earthquake Engineering*. Lisbon, Portugal.

Toan, N. (2014). A novel method for crack detection in beam-like structures by measurements of natural frequencies. *Journal of Sound and Vibration, 333*(18), 4084–4103.

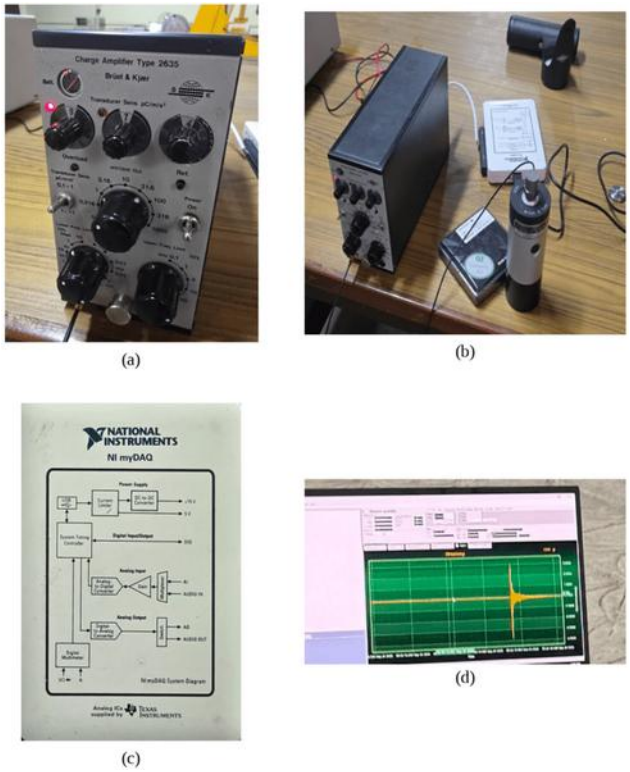
Zhu, W. D., & He, K. (2013). Detection of damage in space frame structures with L-shaped beams and bolted joints using changes in natural frequencies. *Journal of Vibration and Acoustics, 135*(5), Article 051001.

Appendix A

Figure A1 shows the instruments used for the experimental free vibration tests: the charge amplifier, DC power supply, NI data acquisition module and the LabVIEW acquisition screen.

Figure A1

Instruments Used in the Experimental Procedure



(a) (b) (c) (d)

Retrofitting an FDM 3D Printer for Ceramic Additive Manufacturing: A Lead-Screw Extrusion Approach

Arjan Bista[1], Dhirendra Raj Madai[1*]

[1]Department of Mechanical and Aerospace Engineering, Pulchowk Campus, Institute of Engineering (IOE)
Lalitpur, Nepal
[*]Corresponding author: 078bme011.dhirendra@pcampus.edu.np

Abstract

Commercial ceramic additive manufacturing systems remain costly for small-scale research, educational use, and small production runs. This paper presents the design and implementation of a low-cost lead-screw based extrusion pump fitted to a fused deposition modelling (FDM) printer. The stock thermoplastic extrusion assembly was replaced with a piston-based pump. The piston was driven by a T8×8 trapezoidal lead screw (8 mm lead) coupled to a wiper motor through a 1:3 gear reduction. Sealing was achieved using a double O-ring configuration in which the top O-ring acted as a wiper and the second as a standard seal. The pump was sized to hold 1 kg of a mixture of 40% clay and 60% water by weight. The pump body was held under compression by 2 × M6 threaded bolts, while the gearbox was 3D printed and reinforced with a 2 mm metal plate to withstand the large extrusion force of the pump. Extrusion of clay was achieved by providing a constant PWM signal (value 130 of 255, approximately 51% duty cycle) to the motor under a 12 V power supply, while the piston–thread assembly was allowed to slip in a controlled manner to prevent structural failure of the gear assembly. An MKS Gen L V1.0 board (Makerbase) was used as the controller for the FDM printer and PrusaSlicer was used in spiral-vase mode to generate the G-code. Nozzles of 3, 4, and 5 mm were tested, and a 4 mm nozzle with a 2 mm layer height gave the best print results of the configurations tested. Printed vessels were fired in an electric furnace at 1000 °C for 4 hours (heating from room temperature to 1000 °C in 1 hour), cooled in the furnace for a whole day, and visually inspected for cracks, inclusions, and weak interlayer lines. The fired vessels showed no crack lines and no leakage in a water-fill test.

Keywords: ceramic additive manufacturing, clay 3D printing, paste extrusion, lead-screw piston extruder, FDM retrofit

Introduction

Clay 3D printing is an additive manufacturing (AM) process in which a plastic ceramic paste is deposited layer by layer to form a three-dimensional object. Unlike conventional thermoplastic FDM printing, clay extrusion requires the controlled delivery of a highly viscous, non-Newtonian material rather than melting and feeding a solid filament. The extrusion system must therefore generate sufficient pressure, maintain continuous flow, and tolerate variations in moisture content, particle size, and paste consistency.

Commercial ceramic paste printers remain expensive relative to the budgets of small research laboratories, teaching workshops, and craft producers, whereas desktop FDM printers are widely available and inexpensive. A desktop FDM printer already provides a calibrated Cartesian motion platform, stepper drives, endstops, and an open-source firmware and slicing ecosystem. Reusing this infrastructure and replacing only the thermoplastic hot end with a paste extruder

offers a direct route to an affordable ceramic printer, an approach whose feasibility has been demonstrated by Chaari et al. (2022).

The main engineering challenge in such a retrofit is the extruder. Clay paste requires high and sustained extrusion pressure, which in turn demands a high-torque drive, a robust mechanical structure, and reliable sealing, while remaining compatible with the motion controller and the slicer workflow of the host printer. The objective of this work was to convert an existing FDM printer into a functional clay printer using a remotely mounted lead-screw piston pump driven by an automotive windscreen wiper motor. The specific contributions of the paper are:

1. the design of a low-cost lead-screw piston extruder with a 3D-printed, metal-reinforced gearbox, a double O-ring seal, and a controlled-slip overload mechanism;
2. the integration of this extruder with an MKS Gen L controller, Marlin firmware, PrusaSlicer, and Repetier-Host using PWM-based open-loop pump control;
3. an experimental comparison of 3 mm, 4 mm, and 5 mm nozzles for stable clay deposition; and
4. the production and firing of printed vessels to verify that the process yields crack-free ceramic parts that showed no leakage in a water-fill test.

Literature Review / Related Work

Material extrusion of ceramic pastes is generally realised with one of three feeding principles: pneumatic (air-pressure) extrusion, ram or piston extrusion, and screw (auger) extrusion (Alonso Madrid et al., 2023; Chaari et al., 2022). Pneumatic systems are simple and keep the moving mass low, but the compressibility of air makes start–stop response sluggish and flow sensitive to paste rheology. Piston systems displace a defined volume per unit of stroke and can develop high pressures, which makes them well suited to stiff clay bodies, but their capacity is limited by the cylinder volume. Auger systems allow continuous feeding from a hopper but are prone to phase separation and require careful paste formulation (Chaari et al., 2022).

Several low-cost systems have been built by modifying existing thermoplastic printers. Chaari et al. (2022) reported a trial to convert a polymer FDM 3D printer to handle clay materials, showing that the motion platform, electronics, and open-source software of a conventional FDM machine can be retained while the extrusion head is replaced by a paste delivery system. Such conversions keep the cost of the machine low and make ceramic AM accessible for teaching and experimentation, but they also expose limitations of the donor platform: the original carriage is designed for a light hot end, and the stock extruder driver is designed for a stepper motor rather than for the high-torque drives required by clay.

Two practical issues recur in low-cost paste extruders. The first is flow control: many systems operate open-loop, so variations in paste moisture, entrapped air, and tube compliance translate directly into over- or under-extrusion (Alonso Madrid et al., 2023; Santos et al., 2023). The second is structural: the forces needed to push stiff clay through a small orifice can damage printed parts, gears, and seals. The present study addresses these issues within a strict cost budget by (i) mounting a high-capacity piston pump off the carriage, (ii) using an automotive wiper motor as an inexpensive high-torque actuator, (iii) reinforcing the printed gearbox and

introducing a controlled-slip overload path, and (iv) empirically tuning a constant-PWM flow regime matched to spiral-vase toolpaths.

Materials and Methods

System Overview

The clay printer consists of four main subsystems: the reused FDM motion platform, the electronic control system, the external clay extrusion pump, and the nozzle assembly. The motion platform provides coordinated X, Y, and Z movement. The control electronics interpret G-code and drive the printer axes. The piston screw extruder pressurises the clay and pushes it through a flexible tube, and the nozzle deposits the clay bead onto the build surface. The working principle is summarised in Figure 1 and the main system specifications are listed in Table 1.

Figure 1

Working Principle of the Developed Clay 3D Printer

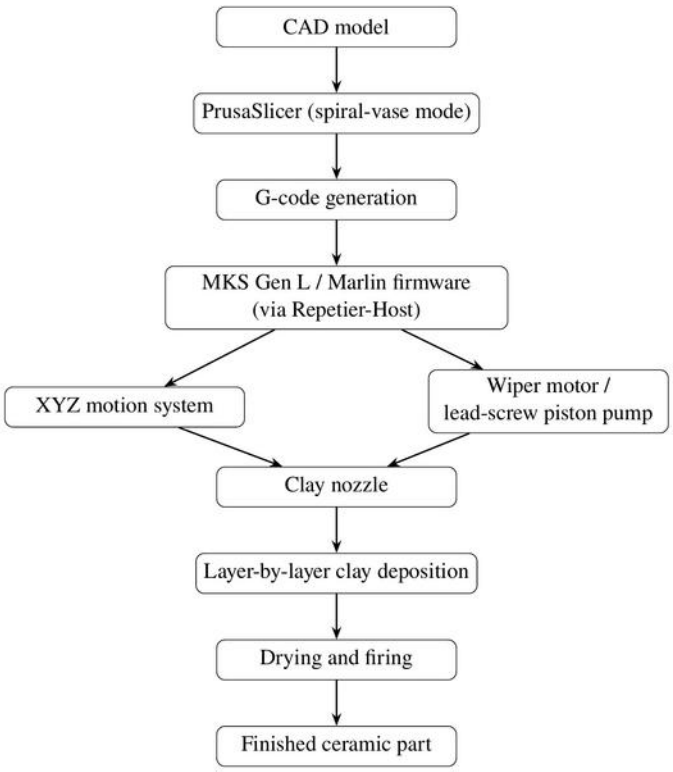


Table 1

Main System Specifications

Parameter	**Value**	**Notes**
Base printer type	Ultimaker clone	Cartesian FDM platform
Controller board	MKS Gen L V1.0 (Makerbase)	Arduino Mega-compatible
Firmware	Marlin	Motion and auxiliary output control
Slicer	PrusaSlicer	Spiral-vase mode
Host software	Repetier-Host	Printer communication and manual control
Extruder type	Lead-screw piston pump	Remote (off-carriage) mounting
Extruder motor	Automotive wiper motor	12 V DC, 1:3 gear reduction
Tube inner diameter	8 mm	PU feed tube
Tube length	500 mm	Pump outlet to nozzle
Best tested nozzle	4 mm	Of 3, 4 and 5 mm tested
Layer height used	2 mm	With 4 mm nozzle
Clay preparation	Fine-filtered clay	De-aired before loading

Mechanical Conversion of the FDM Printer

The original FDM printer structure was used as the mechanical foundation of the clay printer. The frame, guide rails, belts, lead screws, carriage, and build platform were retained. This reuse is advantageous because the FDM printer already provides repeatable positioning, an established coordinate system, and a controller-compatible motion architecture.

The filament extruder and hot-end assembly were removed because clay printing requires neither filament feeding nor thermal melting. In their place, a lightweight nozzle holder was installed on the print carriage. Because the pump is mounted separately, the carriage only carries the nozzle, the tube connection, and its mechanical support, which considerably reduces the inertial load

compared with mounting a full clay reservoir on the moving print head. The key mechanical design considerations were:

- **Nozzle mounting rigidity:** the nozzle must remain fixed relative to the carriage to maintain consistent layer height and bead placement.
- **Tube routing:** the 8 mm tube must be routed to avoid kinking, excessive bending, or interference with axis movement.
- **Build surface clearance:** clay beads are significantly larger than FDM traces, so Z-offset and layer height must be adjusted accordingly.
- **Frame stiffness:** extrusion forces and tube drag can disturb the print head if the mounting is weak.
- **Cleanability:** clay residue must be removable from the nozzle, tube, and build area to prevent drying and clogging.

Figure 2

Retrofitted Clay Printer with Lead-Screw Pump



Lead-Screw Piston Extruder Design

The extrusion system converts the rotation of a wiper motor into the linear advance of a piston that compresses clay inside a cylindrical chamber (Figure 3). The stock thermoplastic extrusion assembly was replaced entirely by this pump. The wiper motor was chosen because it delivers high torque at low speed, is robust, and is cheaply available from automotive sources. Its output drives a T8×8 trapezoidal lead screw (8 mm lead) through a 1:3 gear reduction. The gearbox was 3D printed and reinforced with a 2 mm metal plate to withstand the reaction force generated during extrusion, and the pump body was held under compression by two M6 threaded bolts.

Sealing was achieved with a double O-ring arrangement on the piston: the upper O-ring acts as a wiper that scrapes clay from the cylinder wall, and the lower O-ring acts as a conventional pressure seal. To protect the gear train, the piston–thread assembly was permitted to slip in a controlled manner when the extrusion load became excessive, so that overload is relieved at the thread interface rather than by fracture of the printed gears. The design parameters are listed in Table 2.

The theoretical piston displacement for n revolutions of the lead screw is

(1)

where x is the piston displacement and L is the lead of the screw (axial advance per revolution). For a piston of diameter D, the ideal displaced volume is

(2)

where A is the piston area. To deposit a bead of width w and layer height h at a print speed v (the XY speed of the nozzle relative to the bed), and assuming a rectangular bead cross-section, the required volumetric flow rate and the corresponding screw speed are

(3)

A real bead is closer to a stadium shape than a rectangle, so Equation (3) slightly overestimates the volume demand. In practice, the delivered volume is also lower and less immediate than predicted by Equations (2) and (3) because of clay compressibility, entrapped air, tube expansion, leakage past the seals, and pressure-dependent flow resistance; Equation (3) was therefore used only as a starting point for empirical calibration.

Figure 3

CAD Model of the Lead-Screw Piston Extruder

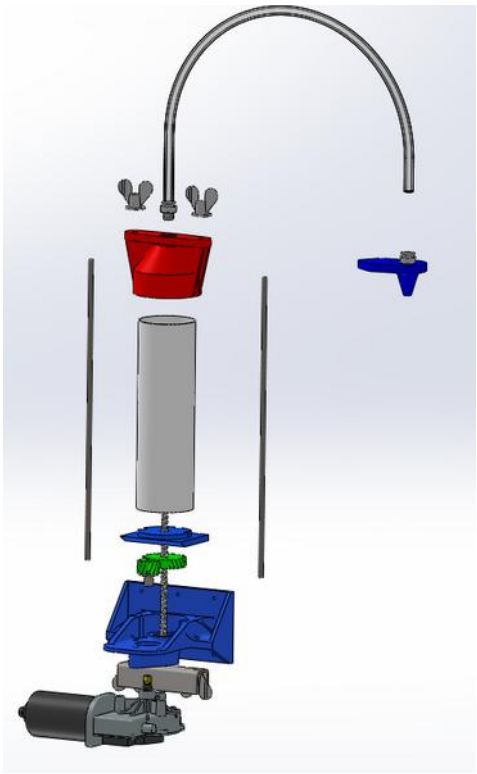


Table 2

Lead-Screw Piston Extruder Design Parameters

Parameter	Value	Notes
Piston diameter	75 mm	Nominal cylinder bore
Piston stroke	150 mm	Maximum active travel
Lead screw	T8×8 trapezoidal	8 mm lead (2 mm pitch, 4-start)
Motor voltage	12 V	DC supply
Motor current	3–5 A normal; 10–12 A stall	Typical wiper motor load profile
Gear reduction	1:3	3D-printed gearbox, 2 mm steel plate reinforcement
Clay chamber volume	662.68 cm³	$V = \pi r^2 h$ with r = 37.5 mm, h = 150 mm
Pump capacity	1 kg	40% clay / 60% water by weight
Outlet connector	PC12-04, 1/2 in	Push-fit connector for flexible tube
Seal type	Double O-ring	Upper: wiper seal; lower: pressure seal
Body clamping	2 × M6 threaded bolts	Holds pump body in compression
Overload protection	Controlled thread slip	Protects printed gear train

Remote Pump and Tube Arrangement

The pump is mounted off the carriage and is connected to the nozzle through an 8 mm tube with a length of 500 mm (Figure 4). The main advantage of this arrangement is that the heavy motor, piston, and clay reservoir do not move with the print head, which reduces the load on the X-axis carriage, helps maintain positioning accuracy, and simplifies refilling and maintenance. The main disadvantage is that the tube introduces compliance and flow delay. When the pump starts, part of the input work is first spent pressurising the clay and expanding the tube before material exits the nozzle; when the pump stops, residual pressure continues to drive clay out of the nozzle, producing blobs and over-extrusion at corners. These effects are more significant for clay than

for molten polymer because paste flow depends strongly on pressure, moisture content, particle distribution, and nozzle resistance.

Figure 4

Pump and 500 mm Tube Connection to the Nozzle



Electronics and Firmware

The printer is controlled by an MKS Gen L V1.0 board (Makerbase) running Marlin firmware. The standard axis motion functions were retained, and the main adaptation concerns the clay pump. Because the wiper motor is a brushed DC motor, it cannot be driven directly from a stepper driver output; instead, a DC motor driver was connected to an auxiliary PWM-capable output of the controller (Figure 5). For the final prints with the 4 mm nozzle, the pump was operated at a constant PWM value of 130 (of 255, approximately 51% duty cycle) from a 12 V supply, which produced a steady extrusion rate. Electrical protection, including fusing, flyback suppression, and proper grounding, is necessary because automotive DC motors draw high transient currents.

Clay printing requires lower accelerations and smoother directional changes than thermoplastic printing, because the wide, wet bead can be stretched, torn, or collapsed by abrupt motion. The acceleration was therefore set well below the usual thermoplastic values. Since the system has no closed-loop flow feedback, pump output was matched to print-head speed empirically. The X and Y stepper drivers were configured with different microstepping settings, which is why their steps/mm values differ in Table 3. The firmware parameters used are listed in Table 3.

Figure 5

MKS Gen L V1.0 Wiring and Wiper Motor Driver Connection

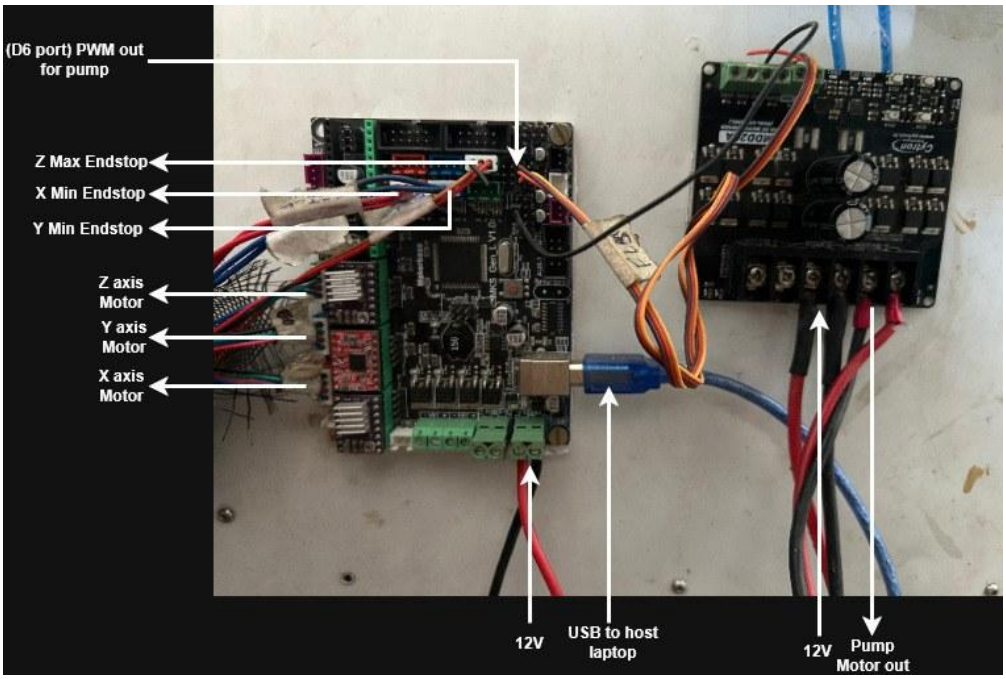


Table 3

Marlin Firmware Settings

Firmware parameter	Value	Notes
X steps/mm	160	Microstepping enabled; differs from Y driver setting
Y steps/mm	80	Different microstepping from X driver
Z steps/mm	800	
Maximum XY speed	60 mm/s	Nozzle speed relative to the bed
Acceleration	1000 mm s^{-2}	Reduced well below thermoplastic defaults
Pump control output	PWM 130 (of 255)	Experimentally determined (approx. 51% duty)

Slicing and Host Software Workflow

PrusaSlicer was used to prepare the print files. The slicer was configured for a large nozzle diameter, thick layers, low accelerations, and no filament retraction. Models were sliced in spiral-vase mode, which, after the solid base layers, produces a single continuous helical wall with no travel moves or start–stop events; this is particularly suited to an open-loop remote pump because it avoids the blobs and gaps caused by pressure lag. Pump start and stop were implemented through custom G-code. Repetier-Host was used to send G-code to the printer and to control the machine manually during homing, jogging, pump priming, and flow testing. The slicer settings are given in Table 4.

Table 4

PrusaSlicer Clay Printing Settings

Setting	Value	Notes
Print mode	Spiral vase	Continuous single-wall toolpath
Nozzle diameter	4.0 mm	Defined in printer profile
Layer height	2.0 mm	50% of extrusion width
Extrusion width	4.0 mm	Matches nozzle bore
Perimeter speed	60 mm/s	XY nozzle speed relative to the bed
Travel speed	60 mm/s	XY nozzle speed relative to the bed
Retraction	Disabled	Replaced by pump stop command
Start pump G-code	M42 P42 S0; M3 S130	Sets motor direction and 130 PWM signal to driver
Stop pump G-code	M3 S0	Removes drive signal

Clay Material Preparation

Fine-filtered clay was used as the printing material. Filtering removes stones, dry lumps, and fibrous contaminants that can block the nozzle or disturb the bead surface. The clay must be wet enough to flow under pressure but stiff enough to retain its shape after deposition: overly wet clay causes walls to slump, whereas overly dry clay increases pump load and leads to intermittent flow and clogging. The mixture contained 40% clay and 60% water by weight. The preparation procedure was:

1. break down dry or semi-dry clay into a uniform slurry or paste;
2. filter the clay to remove oversized particles and hard inclusions;
3. mix thoroughly for 20–30 minutes to distribute moisture evenly;
4. de-air the clay by mechanical or manual vibration before loading;
5. load the piston chamber carefully to avoid trapping additional air pockets; and
6. prime the tube and nozzle until a continuous bead exits before printing.

Table 5

Clay Material Properties

Property	Value	Notes
Clay type	Filtered pottery clay	Fine-grained body, free of heavy grog
Mixture composition	40% clay, 60% water	By weight
Mixing time	20–30 min	Uniform moisture distribution
De-airing method	Mechanical / manual vibration	Removes air pockets before loading
Observed consistency	Creamy, stiff paste	Flows under pressure, retains shape

Nozzle Testing and Calibration Procedure

Nozzles with diameters of 3 mm, 4 mm, and 5 mm were tested. Calibration matched pump output to the motion speed of the printer by observation and repeated tuning. The procedure was: (1) home the X, Y, and Z axes using Repetier-Host; (2) set the nozzle height above the build surface according to the selected layer height; (3) prime the pump until clay exits the nozzle without gaps; (4) print a straight-line test to observe bead width and continuity; (5) adjust the pump PWM until the bead matches the desired line width; (6) print a single-wall cylinder to evaluate layer adhesion and wall stability; and (7) refine the PrusaSlicer speed and layer-height settings as required.

Drying, Firing, and Evaluation

Printed green parts were dried at room temperature for 2–3 days and then fired in an electric furnace at 1000 °C for 4 hours. The furnace was heated from room temperature to 1000 °C in 1 hour. The parts were left to cool inside the furnace for a full day to avoid thermal shock. Fired vessels were inspected visually for cracks, inclusions, and weak interlayer lines, and their waterproofness was tested by filling with water and observing for leakage over 1 hr.

Results

Extruder Performance

The lead-screw piston pump delivered a continuous clay bead through the 500 mm tube at a constant PWM value of 130 (approximately 51% duty cycle). The controlled-slip feature of the piston–thread assembly prevented failure of the 3D-printed gearbox during high-load events such as start-up with a cold, stiff charge or partial nozzle blockage.

Nozzle Comparison

The nozzle diameter strongly affected extrusion pressure, bead width, achievable detail, and reliability (Table 6, Figure 6). The 3 mm nozzle produced finer lines but was more prone to restricted flow and inconsistency. The 5 mm nozzle produced high flow and good clog resistance but reduced print detail and made it difficult to maintain accurate edges on small features. The 4 mm nozzle gave the best overall results of the three tested, providing stable extrusion while maintaining acceptable feature definition and layer bonding; combined with a 2 mm layer height it produced the best prints.

Table 6

Nozzle Test Results

Nozzle diameter	Flow stability	Detail quality	Clogging tendency	Notes
3 mm	Reduced	Fine lines	Higher	Slight under-extrusion
4 mm	Good	Good	Low	Best observed result
5 mm	Good	Reduced	Low	High throughput, loss of detail

Note. Qualitative assessment based on visual inspection of test prints.

Table 7

Calibration Trial Log

Trial	Nozzle diameter	XY print speed	Pump setting (PWM, of 255)	Observations
1	3 mm	60 mm/s	130	High detail, slight under-extrusion
2	4 mm	60 mm/s	130	Optimal flow and excellent layer adhesion
3	5 mm	60 mm/s	130	High throughput, minor loss of detail

Figure 6

Printed Clay Samples Produced Using 3 mm, 4 mm, and 5 mm Nozzles



(a) 3 mm nozzle (b) 4 mm nozzle (c) 5 mm nozzle

Fired Ceramic Parts

After firing at 1000 °C for 4 hours (heating from room temperature to 1000 °C in 1 hour) and a full day of cooling in the furnace, the printed vessels showed no crack lines and no leakage in the water-fill test. No significant inclusions or weak interlayer lines were observed by visual inspection (Figure 7).

Figure 7

Fired Ceramic Vessels Printed With the 4 mm Nozzle at 2 mm Layer Height



Cost

The total cost of the converted printer, including the reused FDM platform components, was NPR 95,859 (excluding VAT). Excluding the donor printer frame, board, shafts, pulleys and belts (NPR 34,400), the cost of the retrofit alone was NPR 61,459. The itemised bill of materials is given in Appendix A (Table 9).

Discussion

The results confirm that a desktop FDM printer can be converted into a working ceramic paste printer with modest modifications, consistent with the conversion reported by Chaari et al. (2022). The key enabler in the present design is the separation of force generation from the print head. A large, remote piston pump driven by a high-torque wiper motor supplies the pressure required by stiff clay without loading the carriage, and the original motion system is therefore left to do what it was designed for.

The choice of a 4 mm nozzle reflects a trade-off between pressure demand and resolution. Because the pressure needed to drive a paste through an orifice rises steeply as the diameter decreases, the 3 mm nozzle pushed the open-loop pump close to the limit at which flow became restricted and inconsistent, while the 5 mm nozzle lowered the pressure demand at the cost of resolution. A layer height of 2 mm (half the bead width) was used to give overlap between successive layers without excessive squashing of the bead, which is consistent with the absence of weak lines after firing. Other layer heights were not tested, so the optimum was not established beyond this setting.

The use of spiral-vase toolpaths was central to obtaining good parts with an open-loop pump. The 500 mm tube and any entrained air make the system respond slowly to changes in pump command, so toolpaths with frequent start–stop events produce blobs and gaps. A continuous

helical path avoids these transients and allows a single constant PWM setting to be used for the entire print. The controlled-slip overload path is a simple but effective way to protect low-cost printed gears; it trades occasional loss of displacement for mechanical robustness. Because spiral-vase mode produces single-wall vessels, the method as demonstrated is limited to this class of geometry.

The production of crack-free vessels that showed no leakage after firing at 1000 °C indicates that the extruded clay maintained sufficient material consistency and interlayer adhesion to retain its structural integrity during firing. The quality of printed ceramic components is influenced by paste consistency, moisture content, and interlayer bonding. Insufficient moisture can contribute to cracking, while excessive moisture may cause deformation or collapse of deposited layers (Santos et al., 2023). Furthermore, air-filled voids within extruded clay structures can compromise their geometry and structural integrity (Jauk et al., 2023; Alonso Madrid et al., 2023). The successful production of the fired vessels therefore demonstrates the suitability of the developed extrusion system and the selected printing parameters for producing functional ceramic objects.

Limitations

The current system has no closed-loop flow control. The controller does not measure clay flow rate, nozzle pressure, piston position, or motor speed, so extrusion depends on empirically tuned relationships between PWM setting and output. Any change in clay viscosity, tube pressure, entrapped air, nozzle resistance, or motor load alters the actual flow rate, which limits repeatability. The 500 mm tube adds pressure lag between pump and nozzle, making start–stop control at corners difficult and restricting the method largely to spiral-vase geometries.

Air bubbles introduced during mixing, loading, or priming absorb pump motion before pressure is transmitted to the clay, causing delayed extrusion, pulsing flow, and oozing after the pump stops. Other practical limitations include nozzle clogging, difficulty cleaning the tube, moisture variation during long prints, and tube drag on the print head. The evaluation of printed parts was largely qualitative and was performed on a limited number of samples of a single clay body. The water-fill test is not a measurement of water absorption, and fired earthenware at 1000 °C may remain porous. The observed issues and possible remedies are summarised in Table 8.

Table 8

Observed Issues and Proposed Remedies

Issue	Observed effect	Possible improvement
No closed-loop flow control	Inconsistent bead width over time	Feedback control using a pressure sensor or motor encoder
Air bubbles	Intermittent flow and gaps in walls	Improved mechanical/manual vibration or vacuum de-airing
Tube pressure lag	Limited start–stop control at corners	Slicer tuning, spiral-vase paths, shorter or stiffer tube
Nozzle clogging	Blocked flow, surface defects on bead	Fine filtering (60–80 mesh) and tapered, polished nozzles
Clay moisture variation	Slumping (too wet) or high pump load (too dry)	Airtight chamber seals and thorough, standardised mixing
Cleaning difficulty	Dried clay blockages in feed tube	Smooth-bore quick-disconnect tubing and flushing after use

Conclusion

A low-cost ceramic additive manufacturing system was developed by retrofitting an existing FDM printer with a remotely mounted lead-screw piston pump. An automotive wiper motor driving a T8×8 lead screw through a 1:3 reduction, a metal-reinforced printed gearbox, a double O-ring piston seal, and a controlled-slip overload path together provided the high, sustained pressure required for clay extrusion without overloading the print carriage. Driven at a constant PWM value of 130 (approximately 51% duty cycle) and combined with spiral-vase toolpaths, the open-loop system produced stable deposition, with a 4 mm nozzle and 2 mm layer height giving the best results among the configurations tested. Printed vessels fired at 1000 °C were crack-free and showed no leakage in a water-fill test, indicating that the approach is suitable for research, education, and low-volume production of single-wall vessels.

Future work should focus on closed-loop pump control using an encoder or pressure sensor, vacuum de-airing of the clay, a shorter and stiffer feed path, optimised nozzle geometry, firmware commands for pump priming and pressure relief, and quantitative characterisation of dimensional accuracy, shrinkage, water absorption, and mechanical strength of fired parts.

Acknowledgments

The authors would like to express their sincere gratitude to Mr. Ramesh Chaudary for his valuable mentorship, continuous guidance, and constructive suggestions throughout the development and completion of this project. His insights and support played an important role in guiding the project and addressing various technical challenges encountered during its implementation.

The authors would also like to extend their heartfelt appreciation to the Ministry of Science, Technology and Innovation, Government of Nepal, for providing financial support and creating a valuable platform to carry out this project through the STEAM Project initiative. This support and opportunity enabled the authors to explore innovative engineering solutions, gain practical experience, and translate theoretical knowledge into a functional prototype.

The authors are also grateful to the Department of Mechanical and Aerospace Engineering, Pulchowk Campus, for providing access to the furnace and allowing its use during the project. Special thanks are extended to the Robotics Club, Pulchowk Campus, for providing the necessary equipment, workspace, and workstation facilities that supported the design, fabrication, assembly, and testing activities.

Finally, the authors acknowledge all individuals who directly or indirectly contributed to the successful completion of this project through their assistance, encouragement, and cooperation.

Funding

This research was financially supported by the Ministry of Science, Technology and Innovation (MoSTI), Government of Nepal, through its Science, Technology, Engineering, Arts, and Mathematics (STEAM) Project initiative. The funding provided support for the development, fabrication, and experimental activities undertaken as part of this project.

Conflict of Interest

The authors declare no conflict of interest.

Author Contributions

Dhirendra Raj Madai: Conceptualization, mechanical design, electronics and firmware; Arjan Bista: Mechanical Design, material preparation, testing, Report writing. All authors reviewed and approved the final manuscript.

Data Availability

Supporting photographs, CAD files, testing videos, and the bill of materials are available in the project repository: https://drive.google.com/drive/folders/1qDv1-6DiULN_zlvHRiJW-zFGiWo6fIhl

Ethical Approval / Consent

Not applicable. This study did not involve human participants, animals, or personal data.

References

Alonso Madrid, J., Sotorrío Ortega, G., Gorostiza Carabaño, J., Olsson, N. O. E., & Tenorio Ríos, J. A. (2023). 3D claying: 3D printing and recycling clay. *Crystals*, *13*(3), Article 375. https://doi.org/10.3390/cryst13030375

Chaari, M. Z., Abdelfatah, M., & Loreno, C. (2022). A trial to convert a polymer FDM 3D printer to handle clay materials. *SN Applied Sciences*, *4*, Article 68. https://doi.org/10.1007/s42452-022-04937-w

Jauk, J., Gosch, L., Vašatko, H., Königsberger, M., Schlusche, J., & Stavric, M. (2023). Filament-reinforced 3D printing of clay. *Materials*, *16*(18), Article 6253. https://doi.org/10.3390/ma16186253

Santos, T., Ramani, M., Devesa, S., Batista, C., Franco, M., Duarte, I., Costa, L., Ferreira, N., Alves, N., & Pascoal-Faria, P. (2023). A 3D-printed ceramics innovative firing technique: A numerical and experimental study. *Materials*, *16*(18), Article 6236. https://doi.org/10.3390/ma16186236

Appendix A: Bill of Materials

Table 9 lists the bill of materials for the clay 3D printer, excluding VAT.

Table 9

Bill of Materials (BOM) for the Clay 3D Printer

Item	Quantity	Amount (NPR)
Existing FDM printer frame, board, shafts, pulleys and belts	1	34,400
PLA filament	8	19,200
Motors	4	7,800
Wiper motor	1	1,800
Power supply	1	1,850
Motor driver	2	3,000
Stepper drivers	4	3,600
LiPo battery	1	5,200
Memory card and USB	1	1,700
PVC pipe	2	1,485
Glass bottle	2	1,600
PU pipe and connector	1	880
O-rings, nuts, bolts and screws	–	1,944
Clay	–	1,400
Miscellaneous	–	10,000
Total (including donor printer)		**95,859**
Total excluding donor printer frame, board, shafts, pulleys and belts		**61,459**

Note. Prices exclude VAT.